Aging Matrix Visualizes Complexity of Battery Aging Across Hundreds of Cycling Protocols

Bruis van Vlijmen[†1,2], Vivek N. Lam[†1,2], Patrick A. Asinger[†3], Xiao Cui[†1,2], Joachim Schaeffer[3,4], Alexis Geslin[1,2], Devi Ganapathi[1,2], Shijing Sun[5], Patrick K. Herring[5], Chirranjeevi Balaji Gopal[5], Natalie Geise[2], Haitao D. Deng[1,2], Henry L. Thaman[1,2], Stephen Dongmin Kang[1], Steven B. Torrisi[5], Amalie Trewartha[5], Abraham Anapolsky[5], Brian D. Storey[5], William E. Gent[1,2], Richard D. Braatz[⋆3] and William C. Chueh[⋆1,2,6]

[1]Department of Materials Science and Engineering, Stanford University, Stanford, CA, USA.
[2]Applied Energy Division, SLAC National Accelerator Laboratory, Menlo Park, CA, USA.
[3]Department of Chemical Engineering, Massachusetts Institute of Technology, Cambridge, MA, USA.
[4]Control and Cyber-Physical Systems Laboratory, Technical University of Darmstadt, 64289, Germany.
[5]Toyota Research Institute, Los Altos, CA, USA.
[6]Department of Energy Science and Engineering, Stanford University, Stanford, CA, USA.

[†]These authors contributed equally to this work
[⋆]Corresponding Author. e-mail: wchueh@stanford.edu; braatz@mit.edu

S.1 Definitions

S.1.1 Mechanistic SOH Metric Definitions

Name	Definition
Cell-level performance metrics	
EFC	Equivalent Full Cycles to EOL. See SI Section S.4.1 for details.
$\mathbf{Q_{RPT,0.2C}}$	0.2C rate-specific capacity
$\mathbf{Q_{RPT,1C}}$	1C rate-specific capacity
$\mathbf{Q_{RPT,2C}}$	2C rate-specific capacity
$\mathbf{R_{ohm}}$	0.01s-0s timescale discharge resistance. At 50% SOC unless otherwise noted. See SI Section S.4.2 for details.
$\mathbf{R_{ct}}$	3s-0.01s timescale discharge resistance. At 50% SOC unless otherwise noted. See SI Section S.4.2 for details.
$\mathbf{R_{p}}$	30s-3s timescale discharge resistance. At 50% SOC unless otherwise noted. See SI Section S.4.2 for details.
$\mathbf{R_{tot}}$	30s-0s timescale discharge resistance. Can also be thought of as the summation of $R_{ohm} + R_{ct} + R_p$ See SI Section S.4.2 for details.
Electrode-specific capacities/SOCs	
$\mathbf{Q_{NE}}$	Negative electrode capacity. Calculated from differential voltage fitting. See SI Section S.4.3 for calculation details.
$\mathbf{Q_{PE}}$	Positive electrode capacity. Calculated from differential voltage fitting. See SI Section S.4.3 for calculation details.
$\mathbf{Q_{Li}}$	Lithium inventory capacity. Calculated from differential voltage fitting. See SI Section S.4.3 for calculation details.
$\mathbf{SOC_{NE,4.0V}}$	Negative electrode SOC taken at the full cell voltage of 4.0V. See SI Section S.4.3 for calculation details.
$\mathbf{SOC_{NE,2.7V}}$	Negative electrode SOC taken at the full cell voltage of 2.7V. See SI Section S.4.3 for calculation details.
$\mathbf{SOC_{PE,4.0V}}$	Positive electrode SOC taken at the full cell voltage of 4.0V. See SI Section S.4.3 for calculation details.
$\mathbf{SOC_{PE,2.7V}}$	Positive electrode SOC taken at the full cell voltage of 2.7V. See SI Section S.4.3 for calculation details.
Trajectory Descriptors	
Knee	Capacity knee indicator. A higher value denotes the presence of a capacity knee. See SI Section S.7.1 for details.
R”	Resistance growth factor. The second derivative of the resistance values, with positive values indicating accelerating resistance growth and negative values indicating decelerating growth. See SI Section S.7.2 for details.
NP Ratio	The ratio of $\mathbf{Q_{NE}}$ and $\mathbf{Q_{PE}}$ at EOL. See SI section S.7.3 for details.

Table S1: **Definition table.** Definitions of all mechanistic SOH metrics abbreviations that are used in this study. See SI Sections S.4 and S.7 for details on how these metrics are calculated.

S.1.2 End of Life

End of life (EOL) is estimated to be when $Q_{RPT,0.2C}$ reaches 80% of the nominal capacity 3.87 Ah (80% of 4.84Ah). This value occurs between diagnostic cycles, so the $Q_{RPT,0.2C}$ is linearly interpolated to find the EFCs (see SI Section S.4.1 for EFC definition) to reach this EOL criterion. All mechanistic SOH metrics at EOL are then calculated by linear interpolation to match this EFC.

S.2 Testing Conditions

S.2.1 Data Cycling and Generation

All cells in this study were harvested from a newly purchased 2019 Tesla Model 3. These 21700 cylindrical cells were manufactured by Panasonic and tested to have a low-rate capacity of 4.84Ah. The positive electrode is NCA (approximately 90-5-5 composition) and the negative electrode is a graphite-SiO_x blend. Cells were cycled in CSZ ZP-16-2-H/AC environmental chambers at a chamber temperature set point of 25°C. These chambers were fit with 4-point contact cylindrical cell fixtures from Korea Thermo-Tech Co. Ltd. assembled by SpectraPower. The cells were cycled using two 96 channel Maccor Series 4000 battery cyclers.

The cells are subject to two types of cycling: aging cycles and diagnostic cycles. The aging cycle consists of a multi-step CC-CV charge and a CC discharge. Information on cycling protocol, parameters varied and their distribution see SI Section S.2.3. The diagnostic cycle consists of three main portions: a reset cycle, a hybrid pulse power characterization (HPPC) cycle [1], and a rate performance test (RPT) sequence. The reset cycle, resets the transient kinetics due to the aging cycles, HPPC probes resistance at different SOC increments, and the RPT extracts rate-dependent capabilities (Fig. 1b). For information on diagnostic cycle protocol see SI Table S2. This cycling data is automatically backed up to an S3 bucket and subsequently processed through the BEEP processing pipeline for use in analysis [2].

S.2.2 Diagnostic Cycle Protocol

Step	Type	Value	Limit	End Condition
	Reset Cycle			
1	Charge CCCV	I = C/7	V $\geq$ 4.2V	I $\leq$ C/35
2	Discharge CC	I = $-$C/7		V $\leq$ 2.7
	HPPC			
3	Charge CCCV	I = C/3	V $\geq$ 4.2V	I $\leq$ C/20
		Repeat:		
4	Rest			t = 1hr
5	Discharge CC	I = 1C		t = 30s
6	Rest			t = 40s
7	Charge CC	I = 0.75C		t = 10s
8	Discharge CC	I = $-$C/3		t = 18min
	Go to step 9 if any discharge step has V $\leq$ 2.7V			
9	Discharge CV	V = 2.7V		I $\leq$ C/20
	RPT			
10	Charge CCCV	I = C/5	V $\geq$ 4.2V	I $\leq$ C/20
11	Discharge CC	I = $-$C/5		V $\leq$ 2.7V
12	Charge CCCV	I = C/5	V $\geq$ 4.2V	I $\leq$ C/20
13	Discharge CC	I = $-$1C		V $\leq$ 2.7V
14	Charge CCCV	I = C/5	V $\geq$ 4.2V	I $\leq$ C/20
15	Discharge CC	I = $-$2C		V $\leq$ 2.7V

Table S2: **Diagnostic cycle protocol.** The protocol consists of a Reset Cycle, HPPC, and RPT portion. CC is constant current and CCCV is constant current followed by constant voltage. The limit indicates the value which will not be exceeded. For example, in Step 1 a charging current of C/7 is applied until the voltage reaches 4.2V. Once at 4.2V, the current does not exceed this value of voltage and instead the current decreases until the end condition of current less than C/35 is reached. Step 8 corresponds to discharging 10% of the nominal capacity. All cycling occurs within an environmental chamber set to 25°C. For the exact cycling protocol, see the Maccor procedure file attached in the data release.

S.2.3 Aging Cycles

Step	Type	Value	End Condition
1	Charge CC	I = CC_1	Charge Capacity = 30% $Q_{nominal}$ V $\geq V_{charge}$
2	Charge CC	I = CC_2	V $\geq V_{charge}$
3	Charge CV	V = V_{charge}	t = t_{CV}
4	Rest		t = 5min
5	Discharge CC	I = $CC_{discharge}$	V $\leq V_{discharge}$
6	Rest		t = 15min

Table S3: **Aging cycle protocol.** Details of each of the steps within the aging cycles. CC_1, V_{charge}, etc. are variables that are modified depending on the testing condition. All cycling occurs within an environmental chamber set to 25°C. For further details on the aging cycle protocol, see the Maccor procedure file attached in the data release.

Cycling Protocol Parameter	Parameter Values
Charge Current Step 1 ($\mathrm{CC_1}$)	0.2C, 0.3C, 0.5C, 0.75C, 1C, 2C
Charge Current Step 2 ($\mathrm{CC_2}$)	0.2C, 0.3C, 0.5C, 0.75C, 1C
Charge Cutoff Voltage ($\mathrm{V_{charge}}$)	3.7V, 4.0V, 4.1V, 4.2V
Charge Constant Voltage Time ($\mathrm{t_{CV}}$)	30min, 90min
Discharge Current ($\mathrm{CC_{discharge}}$)	0.2C, 0.5C, 1C, 2C, 3C
Discharge Cutoff Voltage ($\mathrm{V_{discharge}}$)	2.7V, 3.2V, 3.3V, 3.4V, 3.5V, 3.7V
Diagnostic Cycle Interval	100 cycles, 200 cycles

Table S4: **Aging cycle parameter space.** Overview of cycling conditions tested. Each parameter that was varied across different experiments and their values.

Paper	#Chemistries	#Charging Protocols	#Discharging Protocols	#SOC Windows	#Temperatures	Total #Protocols	Total Cells
This Work	1	21	5	16	1	207	359
Li et al. [3]	1	39	36	58	1	64	225
Diao et al. [4]	1	2	3	1	4	24	192
Luh et al. [5]	1	3	4	3	4	60	180
Severson et al. [6] + Attia et al. [7]	1	117	1	1	1	117	169
Stroebl et al. [8]	1	10	21	32	4	40	147
Zhu et al. [9]	3	3	3	1	3	11	130
Wildfeuer et al. [10]	1	4	4	37	12	89	120
Hoog et al. [11]	1	3	3	17	6	36	116
Geslin et al. [12]	1	1	47	1	1	47	92
Preger et al. [13]	3	1	4	3	3	12	66
Keil and Jossen [14]	1	1	5	15	3	48	48
NASA [15]	1	1	5	4	3	34	34
Saxena et al. [16]	1	1	2	5	1	8	16

Table S5: **Cycling dataset literature overview.** Overview of literature battery cycling datasets highlighting the number of distinct operating conditions tested. For this work, the diagnostic interval is not considered a separate parameter.

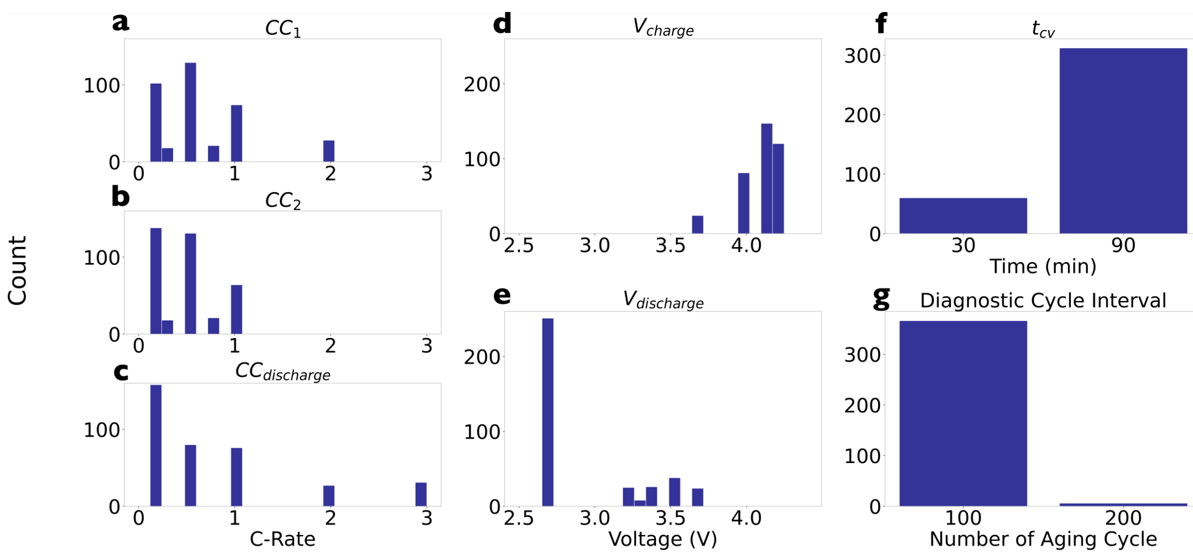

Fig. S1: **Distribution of cycling condition parameters. a-c)** Charging and discharging current histograms plotted in terms of C-rate. **d,e)** Charge and discharge voltage cutoffs plotted in terms of voltage (V). **f)** CV hold time bar plot in terms of minutes. **g)** Diagnostic cycle interval bar plot in terms of number of aging cycles until the next diagnostic cycle.

S.3 State of the Art Comparison

The state-of-the-art methodology to test the influence of a cycling parameter (independent variable) is to fix all other cycling parameters (controlled variables) and vary a single parameter of interest. This methodology definitively gives the impact of the independent variable without the influence of the other controlled variables. However, at different fixed values of controlled variables, the trend of an independent variable can be quite different and non-linear (Fig. S3). To understand the importance of a parameter then, one would need to understand how the parameter influences a metric of interest at all other values of controlled parameters of interest. Exhaustively testing every cycling condition given certain cycling parameters results in an exponentially large number of testing conditions, and is in many cases impractical. Although all testing conditions were not exhaustively tested in this dataset, we instead plot all single parameter trend lines where other cycling parameters are held constant present in this dataset and show these trend lines for three example parameters: V_{charge}, $CC_{discharge}$, and CC_1 (Fig. S3).

The collective response of all of the trend lines provides the importance of a cycling parameter within the bounds of the conditions tested. Still, the trends are difficult to analyze due to the high dimensionality of the dataset (Fig. S3). Instead, we subtract the mean of a trend line (Fig. S3) to better visualize the influence of varying a cycling parameter, and to quantify it we take the mean absolute deviation of each trend lines at the measured data points to get the importance of that feature given a set of other constant parameters. Finally, by averaging all of the trend line's mean absolute deviation we can get a metric for how influential across the dataset varying that cycling parameter is. This metric summarizes the importance of each cycling parameter for an SOH metric of interest within the bounds of the dataset using the data directly. We can then summarize these importance metrics in a matrix plot (Fig. S4a) similar to the random forest SHAP importance matrix plot (Fig. 4b, and Fig. S4b), but with a different metric and methodology. For the most part, both methodologies choose similar most important features with only slight discrepancies.

One major drawback of the mean deviation trend line approach showcased here is that it does not work if it is not possible to hold all other variables of interest constant and selectively vary one parameter. This is the case for calculated/measured features such as using other EOL SOH metrics (Fig. 5) or BOL features (Fig. 6). In these cases, you must use a model to capture the landscape of SOH metric relation to features of interest before attributing feature importances. In this work, a random forest model is used to capture the SOH metric landscape dependence on features, and SHAP is used to interpret their feature importance. Other ML approaches and interpretable metrics could be used depending on what approximates the data best, but a comparison of models is outside the scope of this paper. To conclude, the comparison of our random forest model to an approach rooted in state-of-the-art experimentation of varying one parameter while holding others constant shows similar qualitative feature importances, giving confidence to SHAP value interpretations.

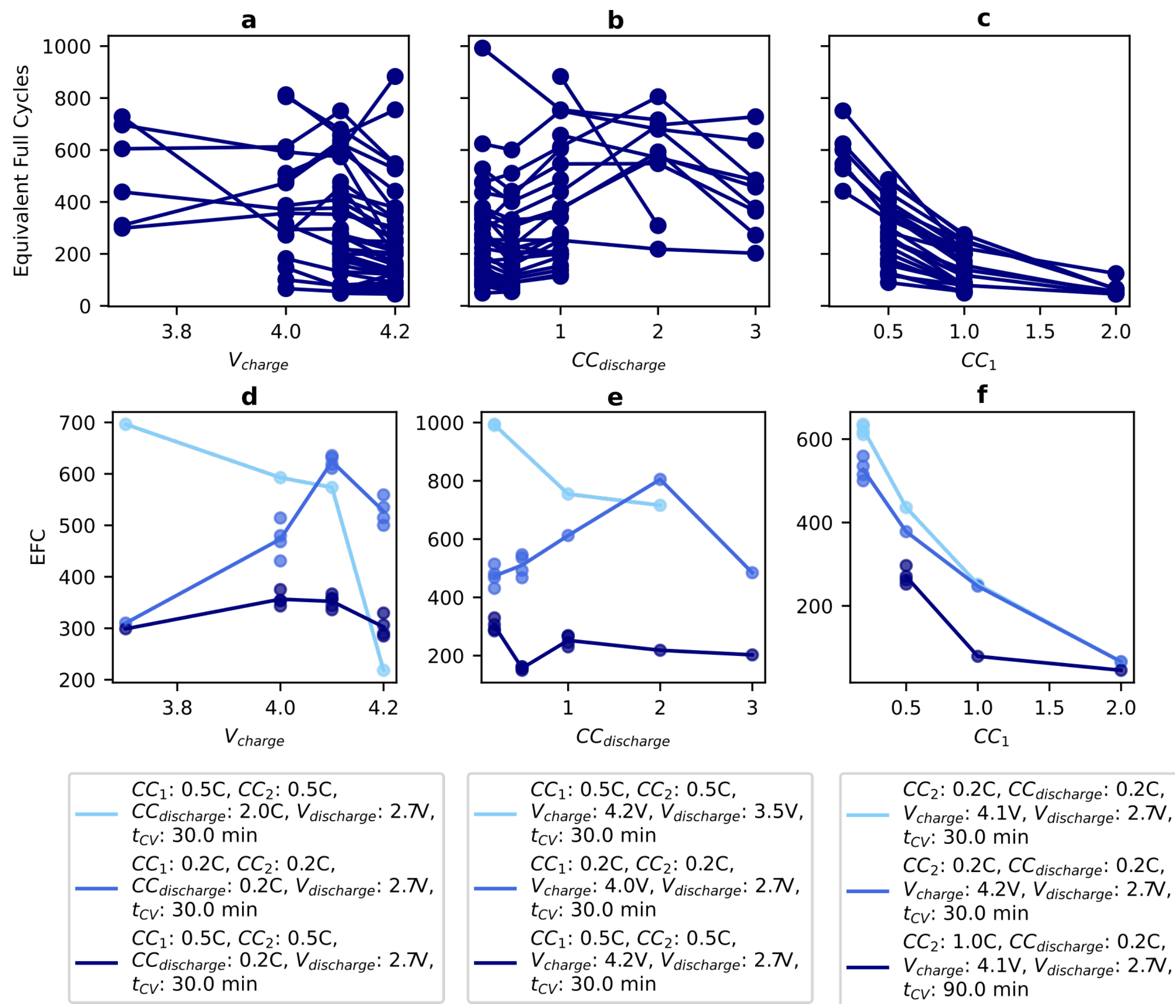

Fig. S2: **Example Trend Lines.** Examples of trend lines where other cycling parameters are held constant and a single parameter is allowed to vary for **a**) V_{charge}, **b**) $CC_{discharge}$, and **c**) CC_1. Only conditions where there are two or more values of the varied parameter of interest are plotted. There are diverse trends based on the values of the other controlled parameters. **d-f**) Specific examples where trend lines show divergent and non-linear trends are showcased for the same three varied parameters of interest shown in **a-c**.

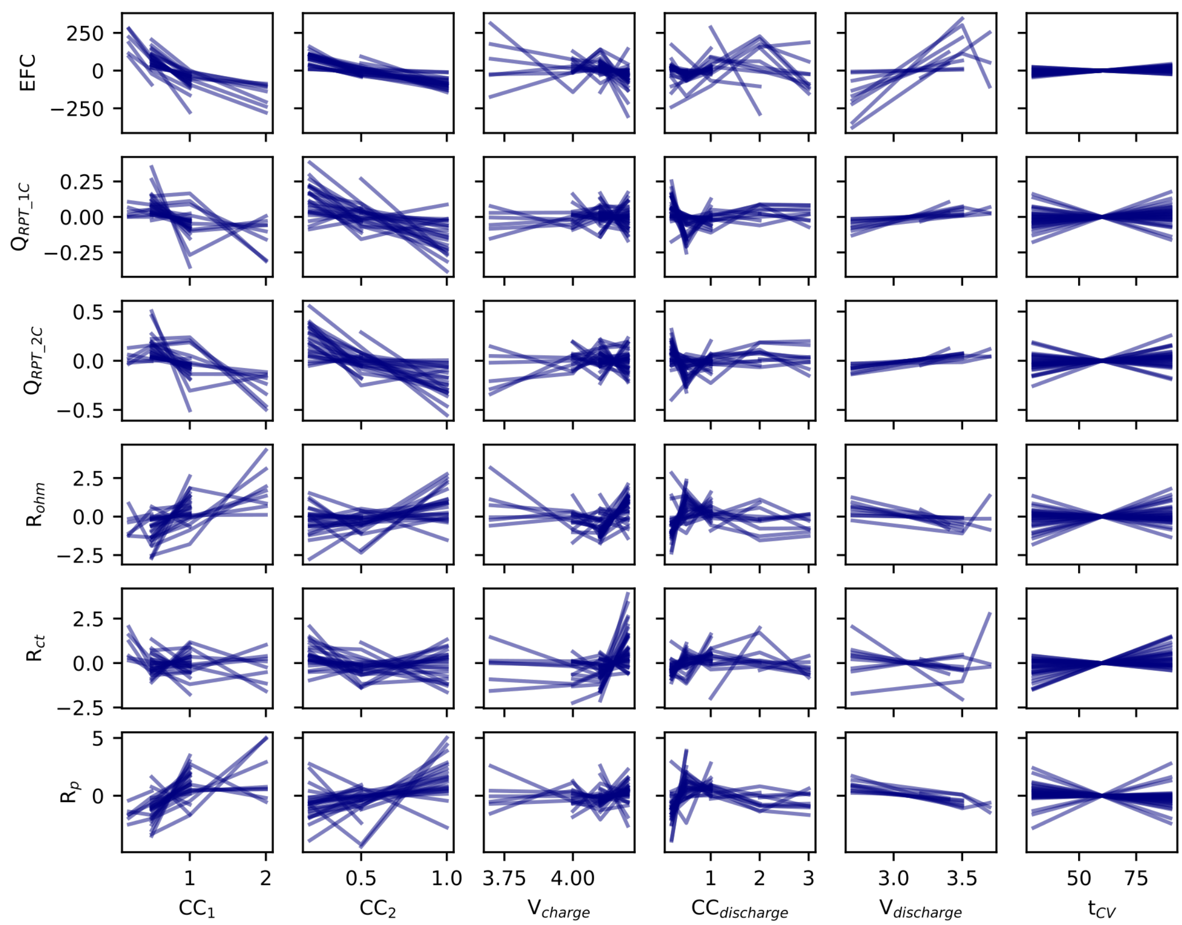

Fig. S3: **Mean Deviation Examples.** Trend lines where the trend's mean is subtracted for comparison. A higher deviation from the mean value indicates a cycling parameter that is more influential given the other cycling conditions.

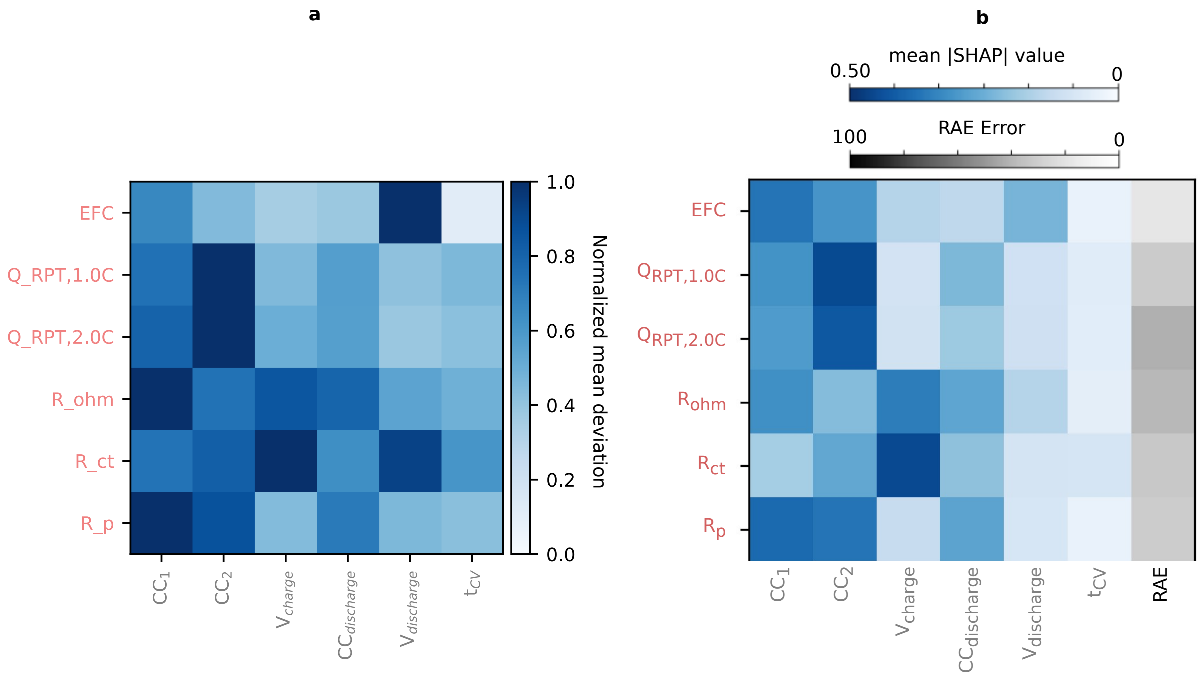

Fig. S4: **Matrix Plot Comparison** Comparison of feature importance derived from **a**) mean absolute deviation of trend lines and **b**) SHAP analysis of RF models used in this paper. Mean absolute deviation values are normalized so that the highest importance is 1 in each row. Both methodologies show qualitatively similar results with some differences.

S.4 Diagnostic Cycle Feature Extraction

S.4.1 Equivalent Full Cycles

Equivalent full cycles (EFCs) are calculated by dividing the total discharge capacity throughput (not including the diagnostic cycles) for a cell by the nominal capacity (4.84 Ah) at a given point in the cell's lifetime. EFCs to EOL is taken as the EFCs interpolated to the point in which the cell reached the EOL condition ($Q_{RPT,0.2C}$ crossing 80% of the nominal capacity).

S.4.2 HPPC Resistance Calculation

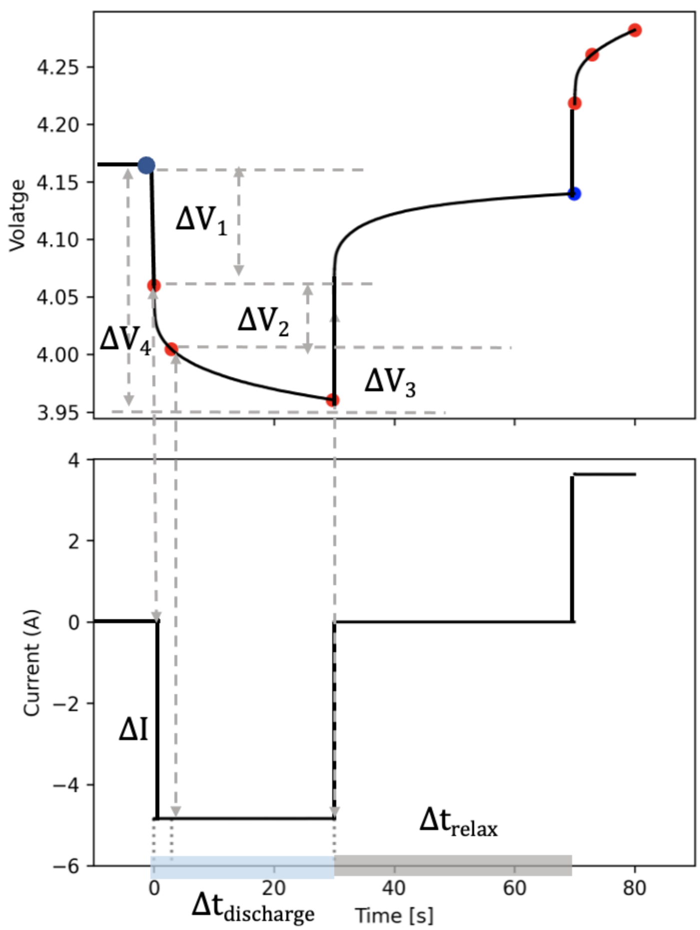

Fig. S5: **HPPC resistance extraction.** Three different time scales are chosen for both charge and discharge resistances corresponding to the red dots in the plots: 0.01s, 3s and either 30s (duration of discharge pulse), or 10s (duration of charge pulse) after applying the pulse. The discharge pulse comes after an hour long rest, while the charge pulse comes after a 40s rest after the discharge pulse. Resistances are calculated using Ohm's Law, taking the overpotential relative to the open circuit voltage (blue dots) before the pulse and dividing by the applied current. We use the 0s to 0.01s resistance as the ohmic resistance (R_{ohm}), 0.01s to 3s resistance to probe the charge transfer regime (R_{ct}), and 3s to the end of pulse to probe the polarization regime (R_p) [17]. The total resistance is taken to be 0s to end of pulse (R_{tot}). Resistances reported in this study are from the 50% SOC discharge pulse unless otherwise noted.

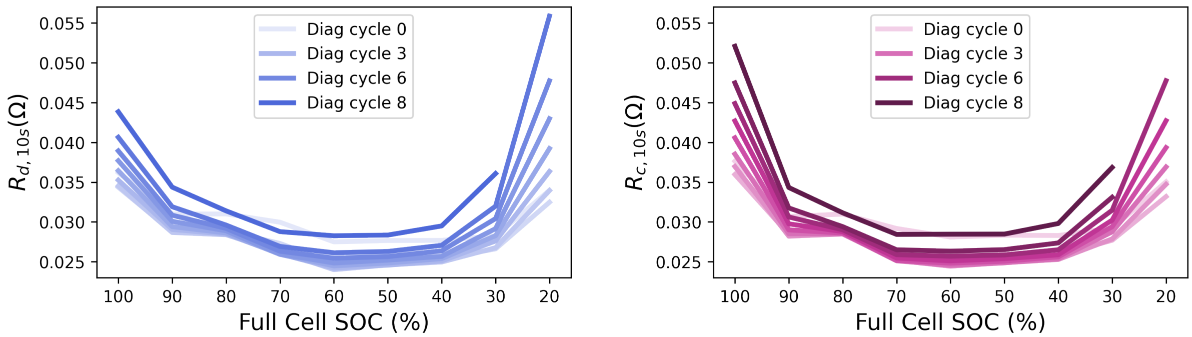

Fig. S6: **Resistance vs. full cell SOC.** Displaying the 10s resistance for charge and discharge plotted against full cell SOC using an example cell (sequence number is 000220). The 10s resistance is chosen since this is the longest time of the charge pulse, this timescale allows comparison of discharge and charge. Color from lighter to darker indicates the progress of cell degradation. Resistance values are higher at SOC extremes, in particular at lower SOC for discharge resistances and at high SOC for charge resistances. Resistance asymmetry is observed at the SOC extremes.

S.4.3 Differential Voltage Fitting for Estimating Electrode Capacities and Offset

Differential voltage fitting (DVF) is used in this work to match the measured C/5 full-cell voltage profile at various SOH to that of an emulated full-cell voltage profile. The emulated full-cell profile is created from reference profiles from the cathode and anode (SI Fig. S7 and SI Section S.5). These reference profiles are shifted and scaled by setting the cathode capacity ($\mathbf{Q_{PE}}$), anode capacity ($\mathbf{Q_{NE}}$), and their offset value (**OFS**), resulting in an optimization with three degrees of freedom. Furthermore, there is the need for a resistance correction, which causes a voltage offset between the emulated full cell and the measured full cell. We correct the emulated full-cell voltage by adding the mean voltage difference between the emulated and measured full-cell voltage. Therefore, this resistance correction does not add another degree of freedom to the optimization. These three parameters fully specify the construction of the emulated full-cell voltage profile (SI Fig. S8). Others have constructed algorithms similar to that used here (e.g., [18–21]).

The DVF fitting procedure used in this work optimizes an objective function that combines the differences between the voltage and capacity derivatives (dV/dQ, dQ/dV) of the emulated and full cell. We found that an objective function that depends on the differential values is more sensitive and yields more reliable results than directly fitting the voltage vs capacity curve. However, we acknowledge that there are many possible objective functions suitable for solving DVF problems.

Based on the solution obtained by the optimization ($\mathrm{Q_{PE}}$, $\mathrm{Q_{NE}}$, and OFS), we can calculate other metrics such as the SOC of each electrode at a particular full cell voltage. $\mathrm{Q_{PE}}$ and $\mathrm{Q_{NE}}$ are directly obtained by the equally named electrode-scaling fitting parameters as shown in Fig. S8. Note that there might be an offset to the true electrode capacities due to the inaccessible lithium problem [22]. The lithium inventory capacity metric, $\mathbf{Q_{Li}}$, is the difference between the maximum capacity value of the rescaled cathode half-cell in Fig. S8 and the minimum value of the rescaled anode half-cell, within capacity domain for which the two electrode curves overlap on the capacity axis. Fig. S8 shows that $\mathrm{Q_{Li}} \geq \mathrm{Q_{FC}}$, as the overlap of the cathode and anode curves extends further right than the vertical dotted line intersecting with the 2.7V on the full-cell curve.

The electrode-specific utilization-window SOCs ($\mathbf{SOC_{PE,2.7V}}$, $\mathbf{SOC_{NE,2.7V}}$, $\mathbf{SOC_{PE,4.0V}}$, and $\mathbf{SOC_{NE,4.0V}}$) refer to the electrode-specific SOCs that match the voltage (2.7 or 4.0V) in the full cell. For example, $\mathrm{SOC_{PE,2.7V}}$ is calculated by finding the discharge capacity at which the full cell is at 2.7V (blue dashed lines in SI Fig. S8), and then calculating the corresponding cathode SOC.

While DVF allows accessing electrode-specific capacities and SOCs, there are several challenges and limitations. DVF only works when the algorithm can accurately reconstruct the measured full-cell voltage profiles with the provided reference half-cell voltage profiles. As the cell degrades, changes in underlying half-cell voltage vs. SOC curves, increased kinetic effects, multi-particle inhomogeneity changes, preferential degradation (such as SiO_x in graphite), and many other phenomena can cause this methodology to yield less reliable results. Additionally, this methodology works best near open circuit voltage conditions to minimize kinetic effects. Although we use C/5 full-cell measurements to shorten diagnostic cycle times, we find that C/5 DVF results correlate highly with C/40 DVF results. However, C/5 and C/40 results agree less well for SOH below 0.85. Further information and discussion can be found in SI Section S.6.

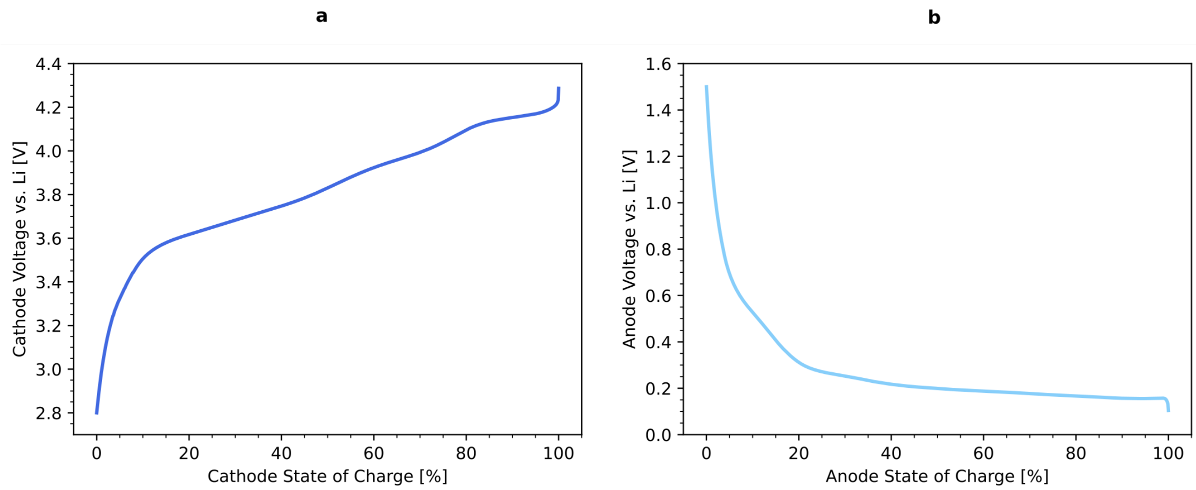

Fig. S7: **Reference voltage profiles.** Reference voltage profiles for the **a**) cathode and **b**) anode. SOC from 0% to 100% is scaled to be the minimum and maximum capacity taken from the half cells. This is defined based on the cycled voltage range: 2.8V–4.3V for the cathode and 0.01V–1.5V for the anode. The half cells used are taken in the direction of discharging for the full cell, lithiation for the cathode and delithiation for the anode. For details on half-cell measurements, see SI Section S.5.

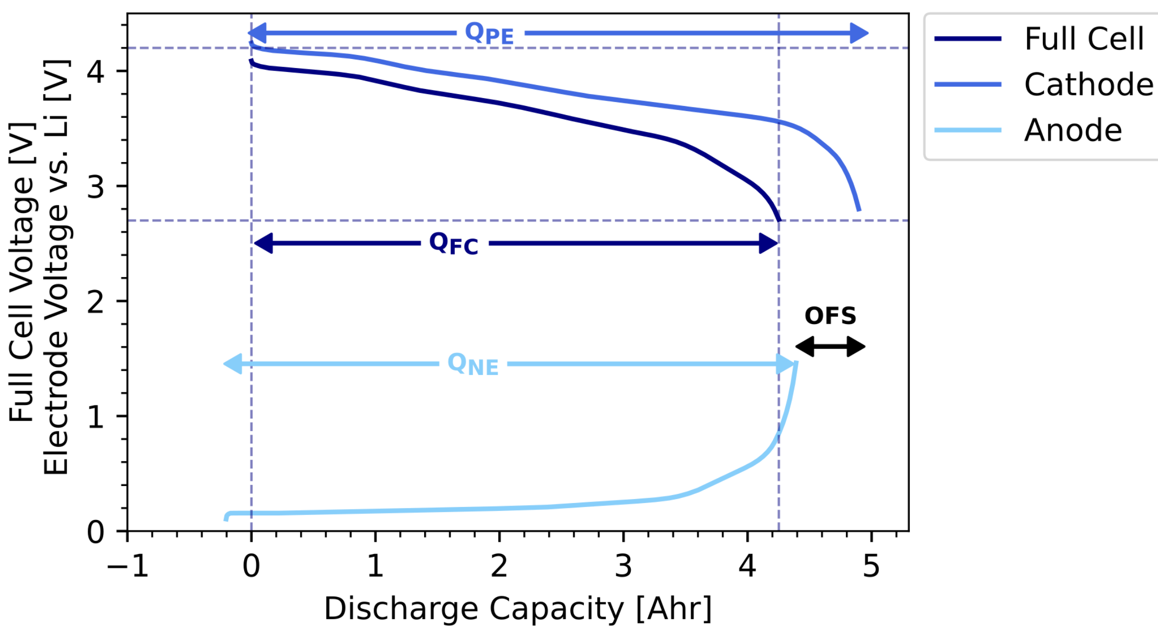

Fig. S8: **Illustration of emulated full cell construction.** Construction of emulated full cell data with $\mathbf{Q_{PE}}$ = 4.9 Ah, $\mathbf{Q_{NE}}$ = 4.6 Ah, and **OFS** = 0.5 Ah. The emulated full cell capacity, $\mathbf{Q_{FC}}$, is the capacity between the voltage limits of 2.7V and 4.2V, which are indicated by horizontal dotted lines. The offset parameter, **OFS**, is the overhang capacity between what is defined as the fully lithiated cathode and fully delithiated anode based on their voltages.

S.5 Half-Cell Voltage Curve Extraction

In order to harvest the electrode material, a 21700 cell was disassembled in an argon-filled glove box (H_2O and $O_2 \leq 0.5$ppm). Prior to disassembly, the full cell was discharged to the lower voltage cutoff (2.7V) to decrease the safety risk in the event of a shorting event. The top cylindrical cell casing cap was removed with pipe cutters. Then a handheld rotary blade (Dremel) was used to score the length of the can to allow for the casing to be peeled open with pliers to extract the jelly roll. Similar cylindrical cell disassembly procedures have been reported in the literature [23, 24].

The NCA and graphite-Si sheets were separated and soaked in dimethyl carbonate to remove residual electrolyte and salt crystals [25, 26]. A lollipop-shaped cutout of the electrode material was then made using a custom die with a manual die cutter (SI Fig. S9b). Due to different binder strength of the NCA and graphite, slightly different procedures were applied to remove the active material from the tab portion of the cutout. For graphite, the tab portion was mechanically delaminated with a plastic razor blade after applying NMP with a cotton swab. For NCA, tape was used to mechanically delaminate the majority of the electrode material followed by gentle cleaning with an NMP soaked cotton swab to prevent tearing of the tab. Care is taken to not remove active material from the active circular region, while removing all the material from the tab region.

Once cleaned, the double-sided electrodes harvested from the full cells were incorporated into pouch cells. The stack geometry is shown schematically in SI Fig. S9a consisting of two shorted lithium metal counter electrodes placed on either side of the double-sided electrode. The electrode stack was then placed into rectangular aluminized pouch material (113PL pouch material, MTI), filled with 200 µl of LP40 electrolyte ($LiPF_6$ in 1:1 by wt. ethylene carbonate: diethyl carbonate from Gotion), and heat sealed on all 4 sides. Hot melt adhesive polymer tape (MTI) was used to create an airtight seal between the pouch material and the current collectors.

Half-cell cycling was performed after a 24-hour rest to allow for sufficient electrolyte wetting. Pouch cells were cycled on Biologic BCS 815 cyclers between lightly hand-tightened pressure plates. These cells were cycled outside of an environmental chamber at room temperature (approximately 25°C). The nominal capacity of the half cell was determined by scaling the full cell nominal capacity by the ratio of the die cut punch out area and the total electrode area. Graphite was cycled at C/40 and 0.15C between 0.01V and 1.5V, and NCA was cycled at C/40 and C/5 between 2.8V and 4.3V.

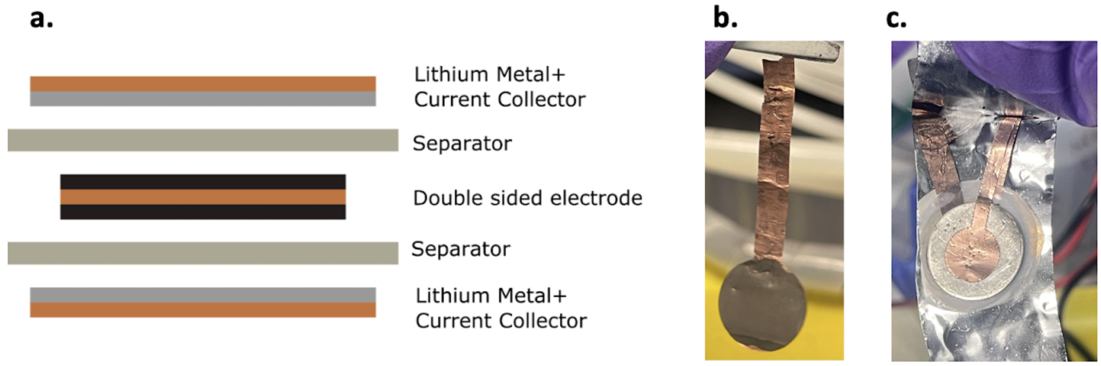

Fig. S9: **Pouch cell preparation. a**) Side view schematic of the half-cell stack with the two lithium counter electrode disks externally shorted together. **b**) Image of a graphite lollipop cutout with the "tail" portion scraped off while the circular active material is kept intact. **c**) Image of pouch cell that has been fully assembled and then cut open to reveal contents.

S.6 Validation of Differential Voltage Fitting Estimates

As explained in SI Section S.4.3, DVF was developed to estimate loss of electrode active material and loss of lithium inventory for quasi-OCV conditions [27]. These methods have been successfully validated experimentally for low C-rates on cells with limited degradation [20]. In our study, we apply the fitting on C/5 discharge voltage data on pristine and aged cells to recover electrode properties estimated throughout the lifetime of the cells. Due to increasing overpotentials, lithiation inhomogeneities, preferential degradation, and other aging induced effects, as the cell degrades DVF accuracy decreases due to an inability to accurately reconstruct the voltage curve [28–30]. Additionally, the collected discharge data at C/5 is significantly higher rate than what is normally used in literature (C/20 to C/40: e.g., [22, 27, 31, 32]). Therefore, we compare DVF results from C/5 to C/40 data from BOL to EOL in this section.

We removed 71 cells at different SOH from the cycling experiment to validate the C/5 DVF fitting with C/40 cycles (SI Fig. S10). We cycled these batteries at C/40 and C/5 before extracting electrode-specific capacities from each profile using the DVF algorithm. We observe a high correlation between the C/5 results for SOH > 0.85 (Fig. S11). However, some challenges remain for the SOH region from 0.85 to 0.8 (Fig. S12). Further experimental validation on degraded batteries is needed to investigate these remaining issues further.

We note that the strong correlation between C/5 and C/40 results is more important than the absolute values, as the degradation trend analysis in this work will remain consistent. Furthermore, the inaccessible lithium problem (see [22]) is affecting both, C/5 and C/40 results.

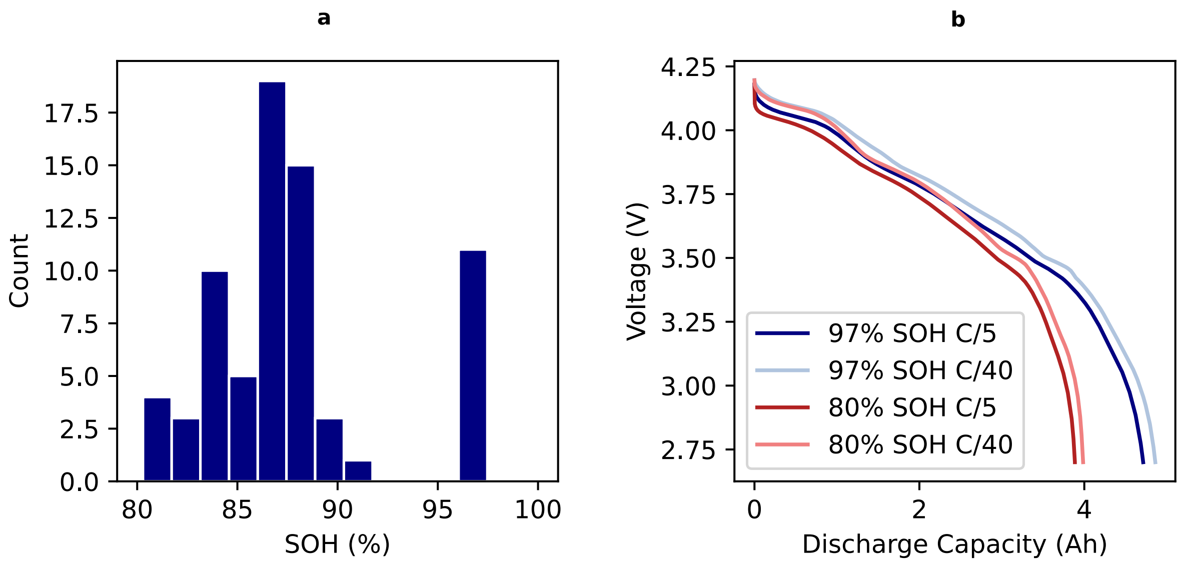

Fig. S10: **Validation cells. a)** Histogram of validation cells SOH. The SOH used here is $Q_{RPT0.2C}$ divided by nominal capacity. **b)** Example C/40 and C/5 data for two cells in this validation dataset near BOL and EOL.

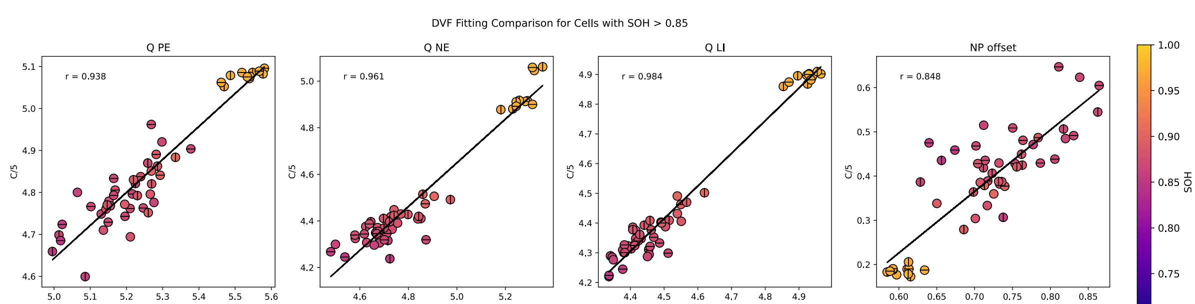

Fig. S11: **Validation of DVF algorithm for cells with SOH > 0.85.** Parity plots with equal axes showing a comparison of our methodology fitting on C/5 data with higher rate half cells vs. using C/40 data fit with C/40 half cells for Q_{NE}, Q_{PE}, Q_{Li}, and NP-offset (OFS). SOH plotted in the color bar is $Q_{RPT0.2C}$ divided by nominal capacity. The Pearson correlation coeffecient is plotted in the top left corner of each plot along with a line of best fit.

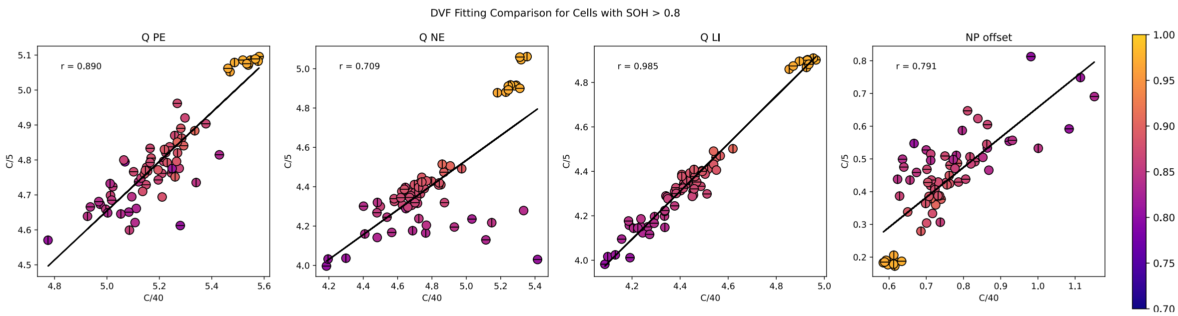

Fig. S12: **Validation of DVF algorithm for cells with SOH > 0.8.** Parity plots with equal axes showing a comparison of our methodology fitting on C/5 data with higher rate half cells vs. using C/40 data fit with C/40 half cells for Q_{NE}, Q_{PE}, Q_{Li}, and NP-offset (OFS). SOH plotted in the color bar is $Q_{RPT0.2C}$ divided by nominal capacity. The Pearson correlation coeffecient is plotted in the top left corner of each plot along with a line of best fit.

S.7 Degradation Trajectories Methodology

S.7.1 Knee Indicator

Similar to common observations in the literature [33], multiple cells in the dataset experience the "knee behavior". Knee behavior is characterized by a capacity fade trajectory with a sudden onset of accelerated degradation. To express two regions of different degradation rates, we fit the capacity loss curve with two linear segments of different slopes with a Bacon-Watts fitting method [34]. This methodology can extract the onset (x_t) of the knee as well as the severity of the knee (Fig. S13 and Equations S.1-S.3). The *knee indicator* is taken to be the knee angle difference to show the severity of the knee (Equation S.3).

$$m_1 = \frac{y_t - a_0}{x_t} \tag{S.1}$$

$$m_2 = \frac{a_f - y_t}{x_f - x_t} \tag{S.2}$$

$$\text{Knee Indicator} = \arctan(m_1) - \arctan(m_2) \tag{S.3}$$

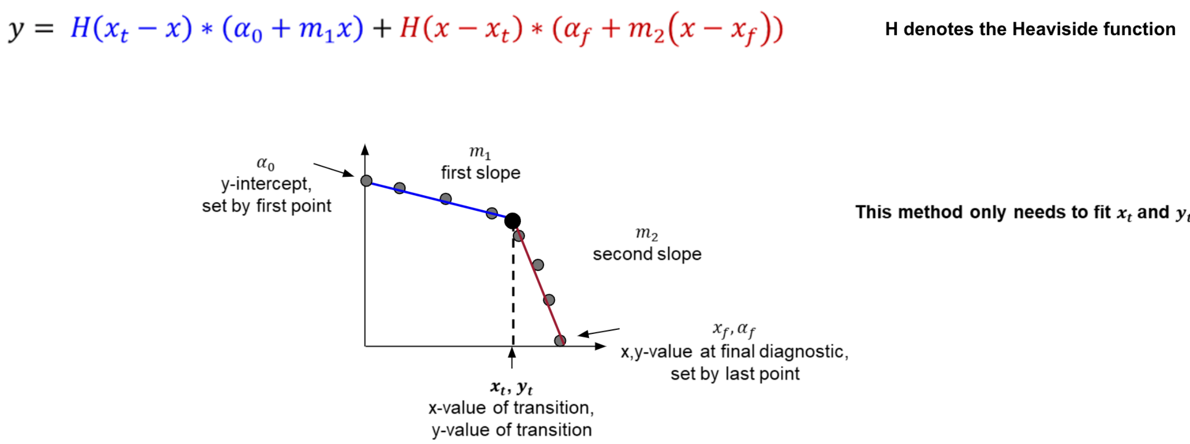

Fig. S13: **Knee indicator fitting.** Schematic depiction of Bacon-Watts fitting method to find the knee onset and knee angle change. The knee angle change is used as the knee indicator with a positive value indicating accelerated degradation.

S.7.2 Resistance Growth Metric

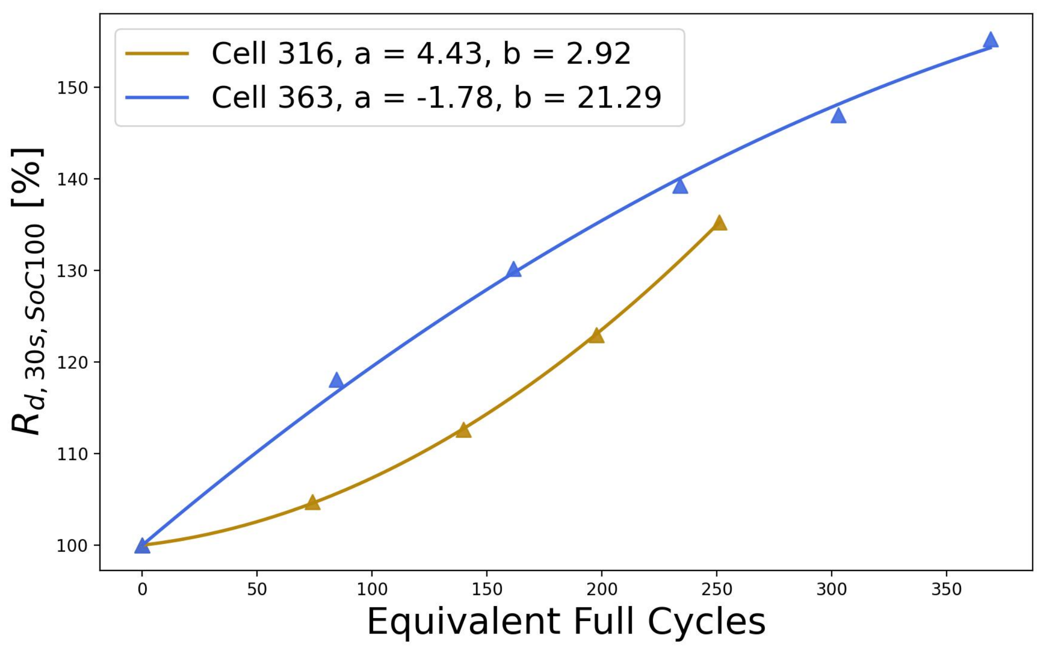

Fig. S14: **Resistance growth factor.** Polynomial curve fitting of the 100% SOC discharge R_{tot} to find the resistance growth factor.

In Fig. 2, we observe that, throughout the dataset, a bisection can be made between cells for which the resistance growth attenuates or accelerates with degradation. This second derivative of resistance can be a characteristic of certain degradation mechanisms, as seen in various prior studies [35]. To capture this, we track the discharge R_{tot} at 100% SOC ($R_{d,30s,SOC100}$). We fit this resistance growth trajectory with a polynomial of the form $ax^2 + bx$ starting from the second diagnostic cycle. We start from the second diagnostic cycle because we typically observe an initial decrease of resistance in first few cycles of aging, likely due to electrode wetting or temperature conditioning (Fig. 2a). The resistance growth factor is the value of the a parameter where $a > 0$ indicates accelerating resistance growth and $a < 0$ indicates attenuating resistance growth. We refer to this value a as the Resistance growth factor, or R", throughout the paper.

When analyzing the Resistance growth factor across the entire dataset, we observe that the majority of values for R" exist just above or below 0. This is as expected, as $R" = 0$ suggests linear resistance growth. Some cells however, experience accelerated resistance growth and sudden failure. These types of degradation inhibit the ability for the Resistance growth factor equation to capture the evolution of Resistance adequately, as they do not conform to the $ax^2 + bx$ description.

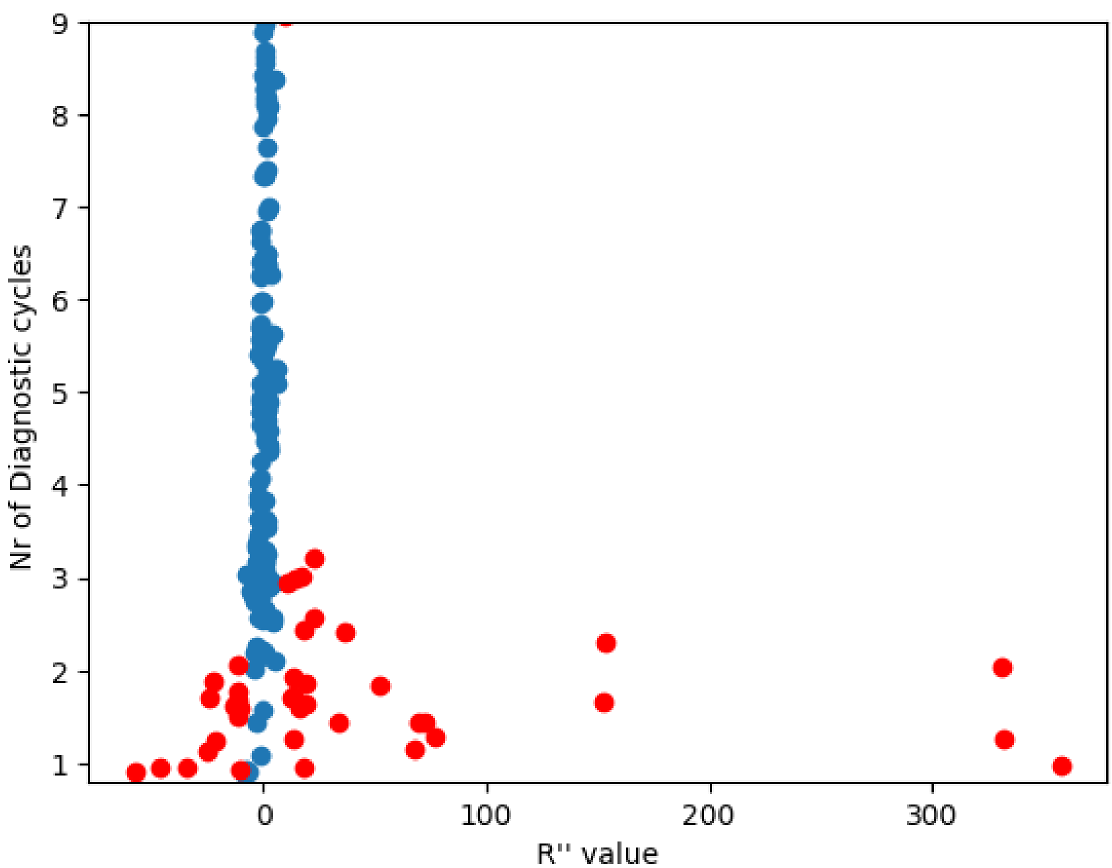

Fig. S15: **Resistance Growth Factor R sensitivity to number of datapoints"**. Values of R", i.e. a in $ax^2 + bx$, seem to fall in a range of -10 to 10, once there are 4 or more Diagnostic Cycle datapoints to fit on.

We are fitting a 2nd-order polynomial $ax^2 + bx$, on the $\mathrm{R}_{\mathrm{d,30s,SOC100}}$ Resistance data starting from the second order diagnostic cycle. In order for the empirical data to adequately fit this polynomial, you need sufficient data. Theoretically, you'd need a minimum of 2 data points to fit in $ax^2 + bx$. As is visible from figure S15 the cells that only have 2 or less diagnostic cycles to fit on will have *R"* values with a large spread. For cells that have at least 3 datapoints to fit on, we see a convergence of *R"* values between 10 and 10.

Therefore, we apply a cut-off on the SHAP-analysis dataset, of R" = 10, as shown in figure S16. This cut-off rejects 41 cells from the dataset.

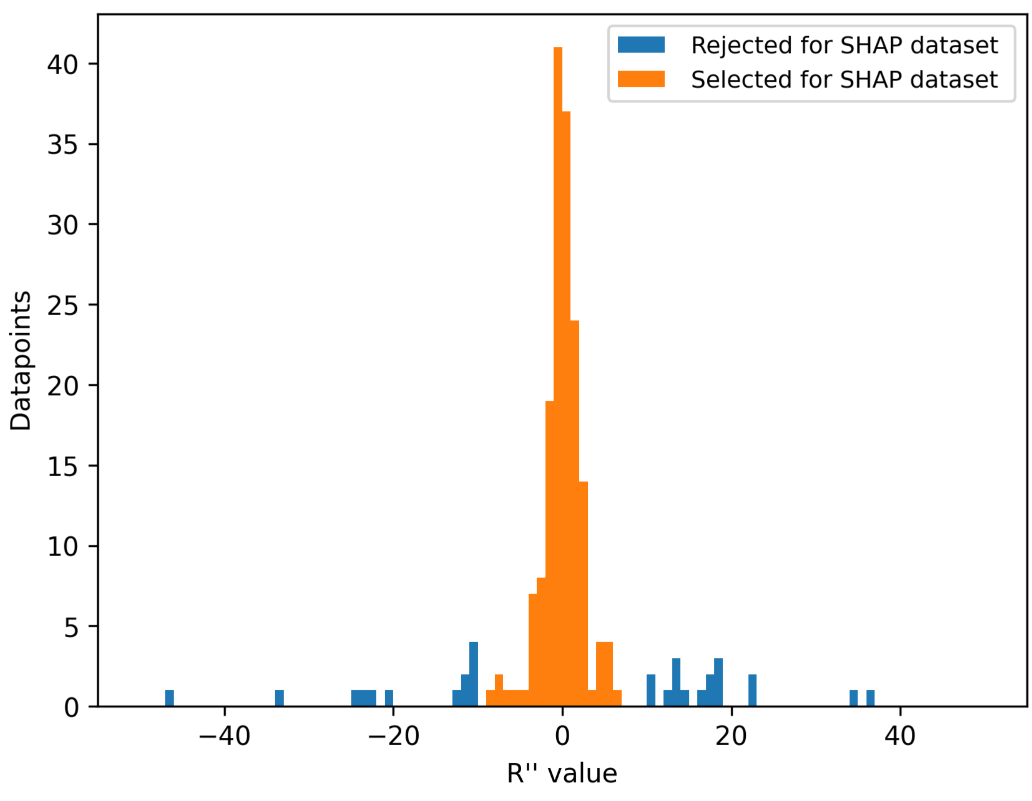

Fig. S16: **Downselection of SHAP dataset for Resistance Growth Factor R"**. Values of *R"*, i.e. a in $ax^2 + bx$, that have a larger absolute value than 10 are rejected for the SHAP analysis dataset.

S.7.3 N-P Ratio

The N-P ratio is a metric that is commonly used to express the ratio between the capacity of the anode (N) and cathode (P). In battery cell design, the N-P ratio is designed such that the graphitic anode is slightly oversized, such that it has more capacity than the cathode. The ratio of Q_{NE} to Q_{PE} is therefore an indicator of the cell balance between both electrodes. When the N-P ratio deviates strongly from its initially designed value, the cell becomes unbalanced and could bring additional stress to one of the electrodes. We calculate the N-P ratio from the ratio of $\mathrm{Q_{NE}}$ and $\mathrm{Q_{PE}}$ at EOL.

S.8 Variability from Beginning-of-Life to End-of-Life

To quantify the variability of key health metrics at BOL and EOL, we present their distributions (Fig. S17). By presenting these SOH metrics, we decompose the variability in full cell performance into the variability of different mechanistic SOH metrics.

BOL results prior to cycling aging are extracted from the first diagnostic cycle. The variability at BOL is narrow for most health indices, having a coefficient of variation in the range of 1% (Fig. S17a-e). Prior to BOL, the batteries spent different amounts of time at room temperature before starting cycling experiments, therefore the initial distributions contain a combination of fundamental manufacturing variability as well as calendar aging effects (SI Fig. S19). The calendar aging effects appear to be negligible compared to the cell-to-cell variability at BOL.

The EOL distributions emphasize the need to report a more holistic view of the SOH of the batteries. At EOL, despite having the same $\mathrm{Q_{RPT0.2C}}$, each battery has a very broad distribution of other mechanistic SOH metrics with several coefficients of variation increasing by an order of magnitude (Fig. S17f-j). This highlights the importance of reporting and tracking multiple metrics; while one metric might be identical, there are several other factors that make up the SOH of a battery. Even under identical cycling conditions, large standard deviations of capacities and resistances are seen at EOL (SI Fig. S18). These broad variabilities and shifting distributions indicate that a complex combination of cycling conditions and initial variability has led these batteries to follow a diverse range of SOH trajectories to EOL.

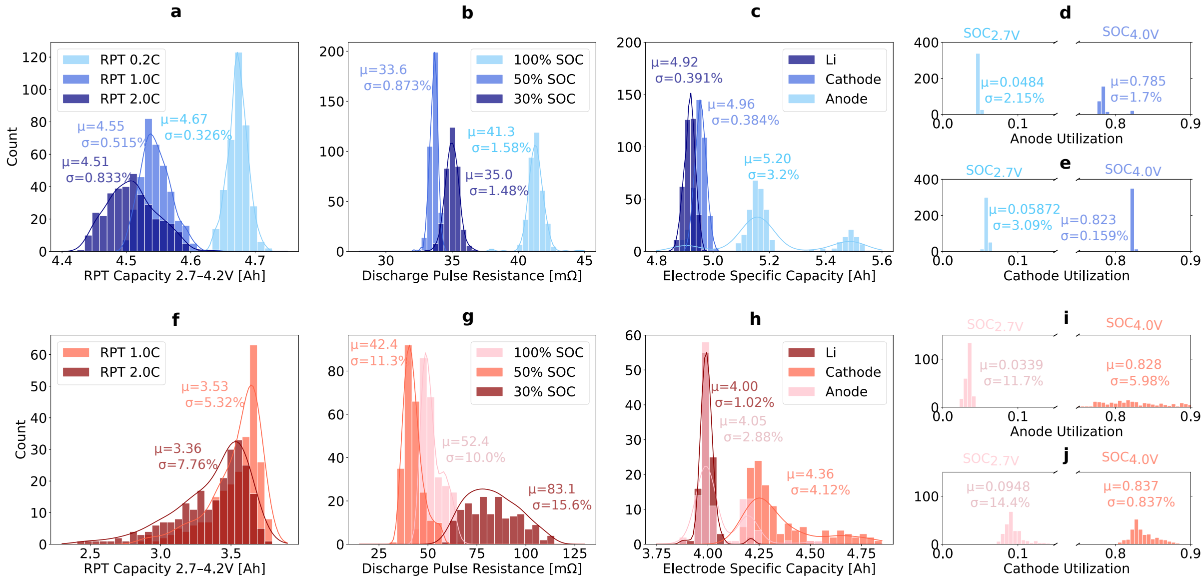

Fig. S17: **Distribution of BOL and EOL mechanistic SOH metrics.** Distribution of BOL (**a-e**) and EOL (**f-j**) mechanistic SOH metrics. The means (μ) and coefficient of variations (σ) are placed within the figure. The distributions are shown for **a,f**) discharge capacities, **b,g**) R_{tot} at 3 different SOCs, **c,h**) electrode-specific capacities, **d,i**) anode electrode-specific SOCs at beginning of discharge (BOD) and end of discharge (EOD), **e,j**) cathode electrode-specific SOCs at beginning of discharge (BOD) and end of discharge (EOD). In **f**, $Q_{RPT0.2C}$ is not plotted as it is used to determine the EOL condition.

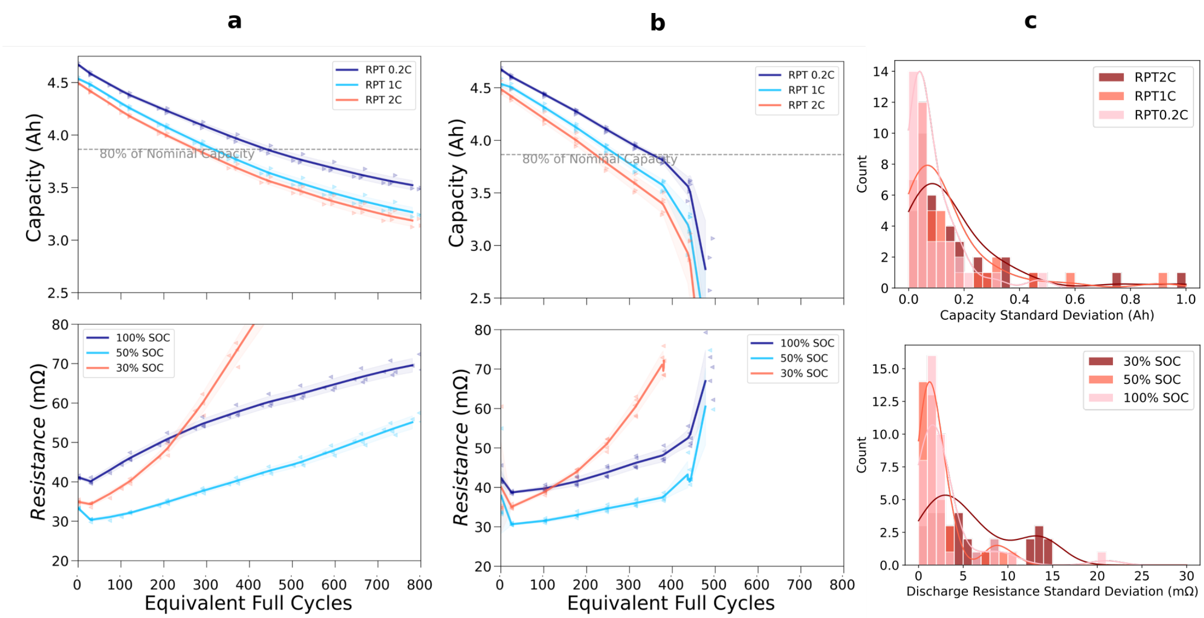

Fig. S18: **Variability of identical cycling conditions.** Plots of the variability of cells cycled under identical cycling conditions. **a,b**) Two example cycling conditions with $\geq$2 cells are shown. Scatter markers show individual data points while the solid line is the mean trajectory. **c**) Histograms showing the standard deviation of RPT capacities (top), and R_{tot} at different SOCs (bottom) at EOL. EOL here is defined for a protocol as the point where the mean of the protocol's $Q_{RPT0.2C}$ crosses 80% of nominal capacity and is not based on individual cells. Each count represents a cycling protocol with $\geq$2 cells at EOL. Even under identical cycling conditions, there exists large variability in the cells' EOL cell-level performance metrics.

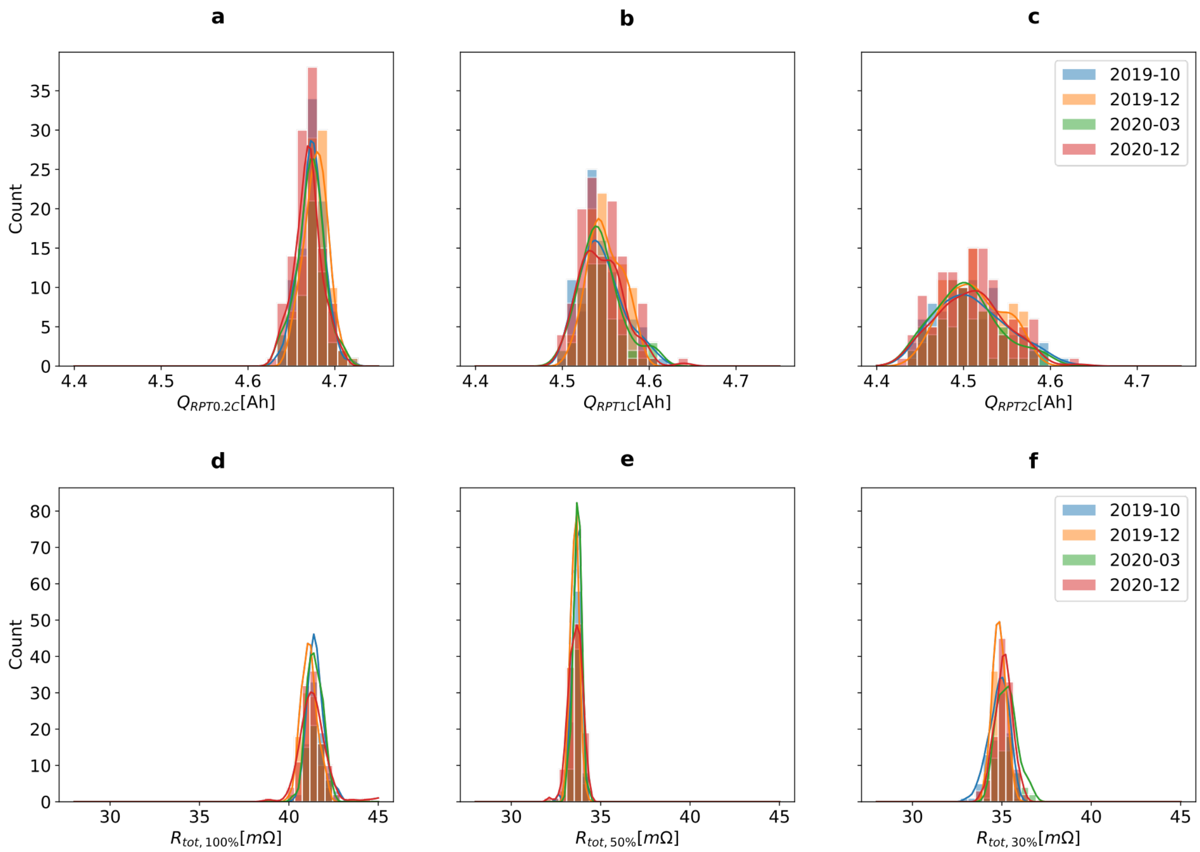

Fig. S19: **Influence of calendar aging on BOL.** The influence of the start time on cell-level performance metrics for **a**)$\mathrm{Q_{RPT0.2C}}$, **b**) $\mathrm{Q_{RPT1C}}$, **c**) $\mathrm{Q_{RPT2C}}$, **d**) $\mathrm{R_{tot,SOC100\%}}$, **e**) $\mathrm{R_{tot,SOC50\%}}$, **f**) $\mathrm{R_{tot,SOC30\%}}$. The batteries used in this study include initial cell-to-cell variability in combination with calendar aging but, as shown here, the calendar aging has no clear observable trend on the distribution of the data.

S.9 Explanatory Models

S.9.1 Input Parameter Correlation for Explanatory Models

We visualize the Pearson correlation coefficients between input parameters using the heat map in Fig. S20 as highly correlated features can lead the model to report misleading feature importance. We note the high correlation between electrode capacities ($\Delta\mathrm{Q_{NE}}$, $\Delta\mathrm{Q_{PE}}$, and $\Delta\mathrm{Q_{Li}}$), but since electrode capacities are not the top important features, this will not affect our conclusion. We point out the highest correlation is between $\Delta\mathrm{SOC_{NE,2.7V}}$ and $\Delta\mathrm{SOC_{PE,2.7V}}$ (Pearson coefficient of -0.93). As shown in Fig. S21, these two features can both appear as the most important, and we argue both in the main text and in Section S.9.2 that only $\Delta\mathrm{SOC_{PE,2.7V}}$ has a real effect on resistance growth and $\Delta\mathrm{SOC_{NE,2.7V}}$ has an artificial trend produced by the nature of its calculation.

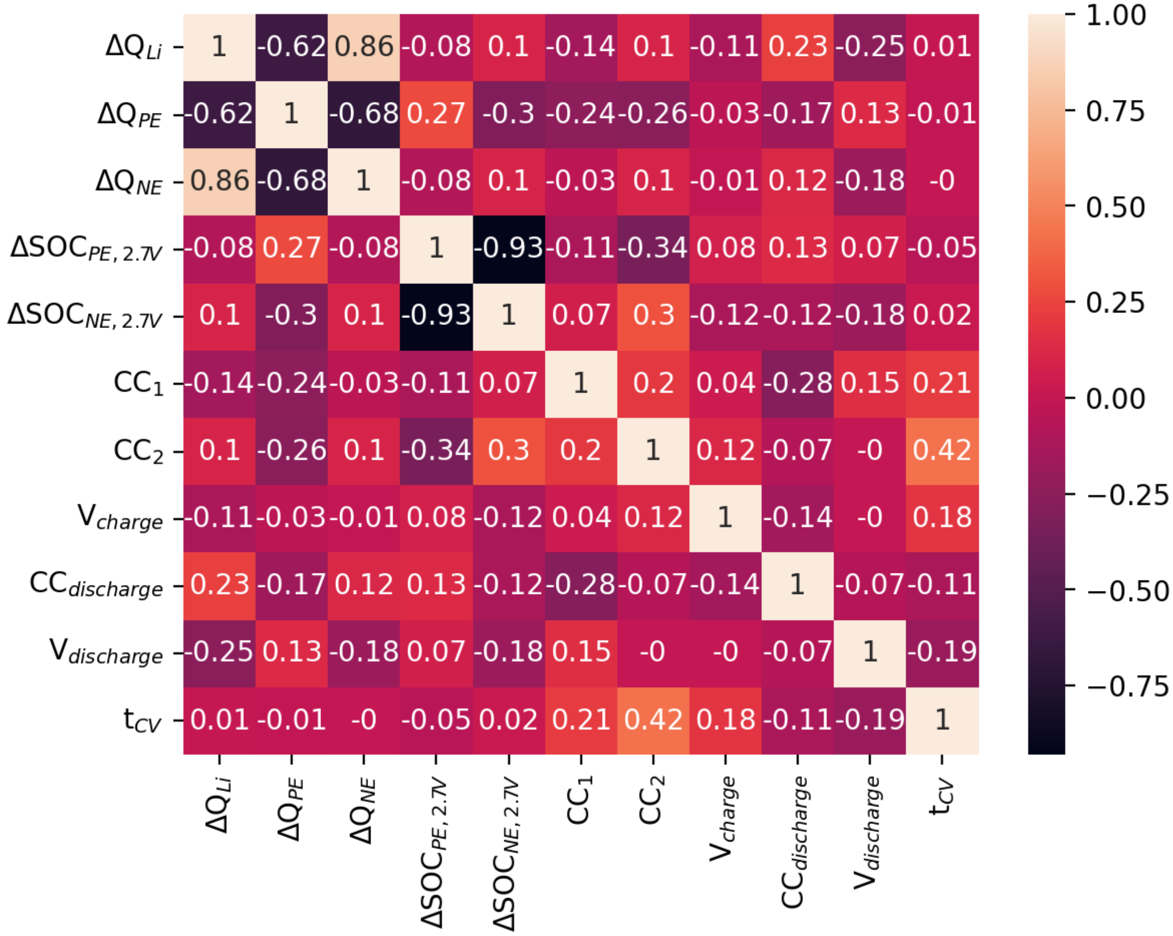

Fig. S20: **Explanatory model feature correlation.** Pearson correlations between input parameters in explanatory model. Correlation between $\Delta\mathrm{SOC}_{\mathrm{NE,2.7V}}$ and $\Delta\mathrm{SOC}_{\mathrm{PE,2.7V}}$ is the highest.

S.9.2 Evidence of PE SOC Influence on Resistance

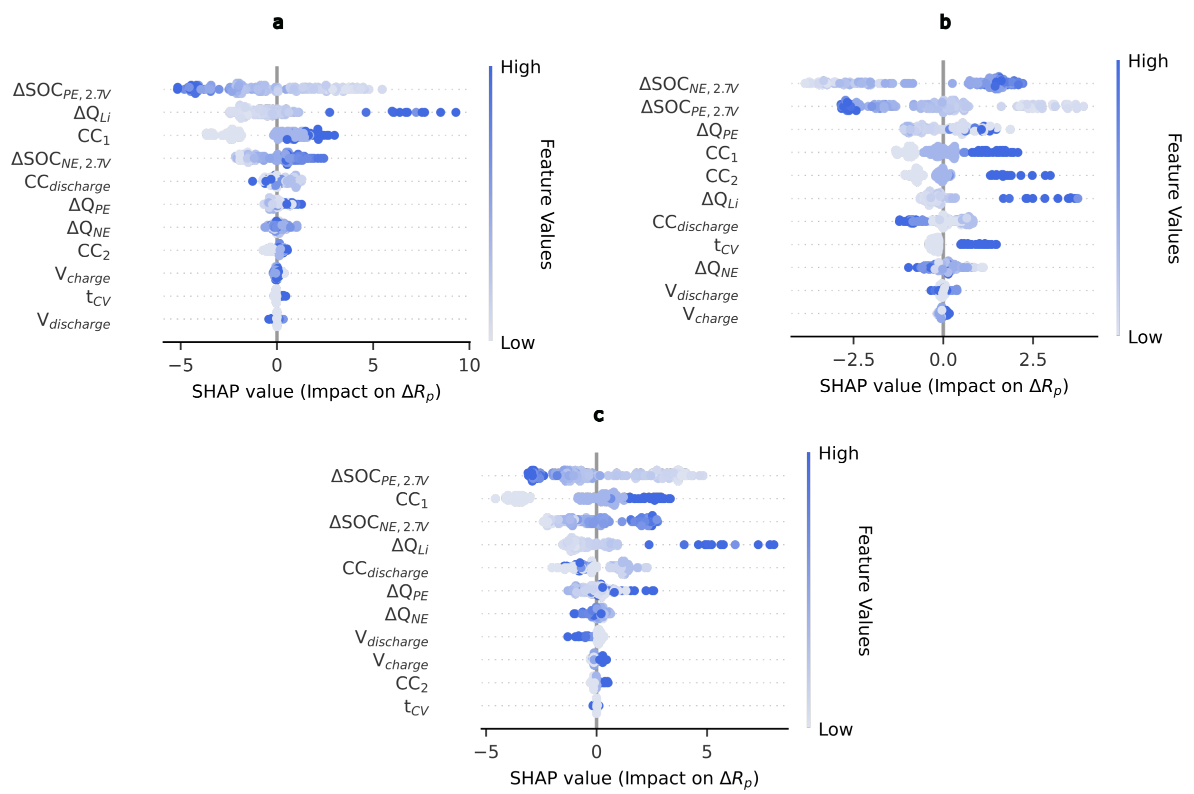

Fig. S21: **Repeat model influence on feature importance.** Three random models to predict ΔR_{tot} generated with different top ranking feature importances. We can see that depending on the model built $\Delta SOC_{PE,2.7V}$ or $\Delta SOC_{NE,2.7V}$ can emerge as the most important feature.

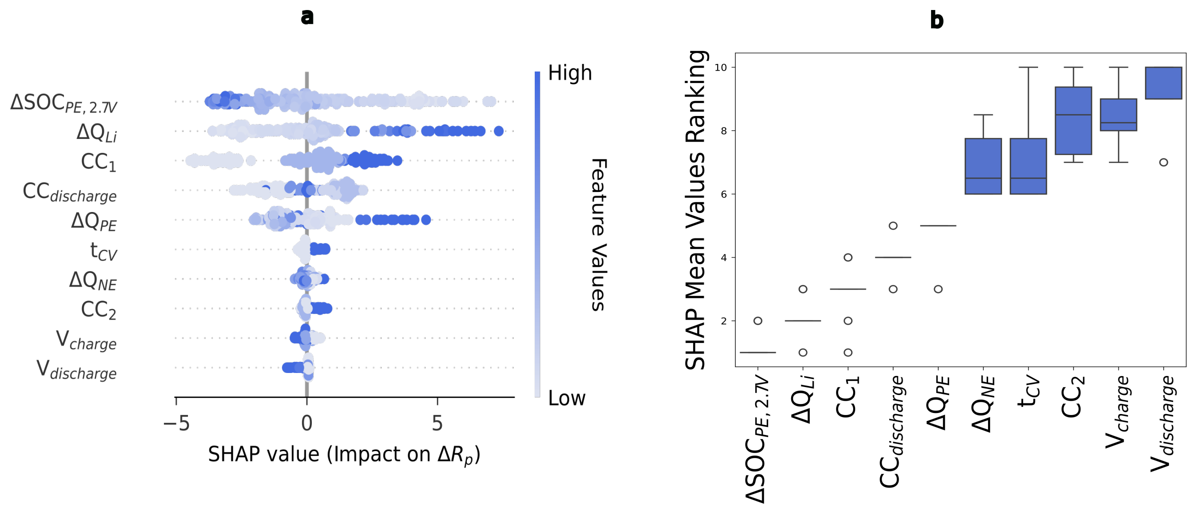

Fig. S22: **Feature importance without anode SOC.** The explanatory model was built without $\Delta\mathrm{SOC}_{\mathrm{NE,2.7V}}$ to observe what the feature importance would be. **a**) One example SHAP beeswarm plot showcasing $\Delta\mathrm{SOC}_{\mathrm{PE,2.7V}}$ as the top feature. **b**) Box plot of feature importance ranking made from explanatory model with 10 different random seeds. Despite the variation in feature importance of other input variables, $\Delta\mathrm{SOC}_{\mathrm{PE,2.7V}}$ always shows up as the dominant feature (rank 1).

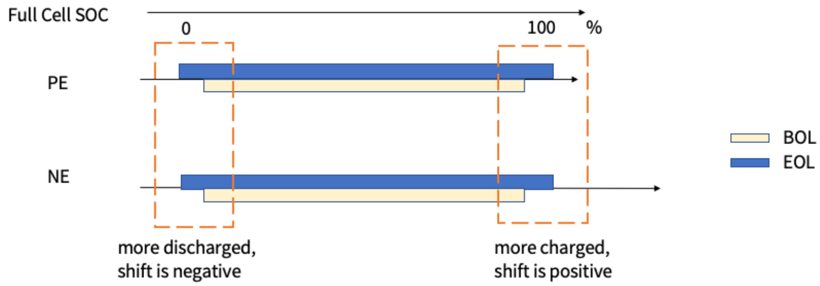

(a)

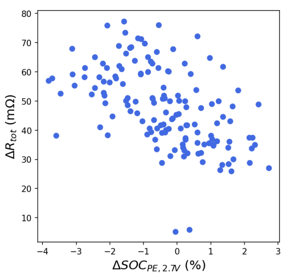

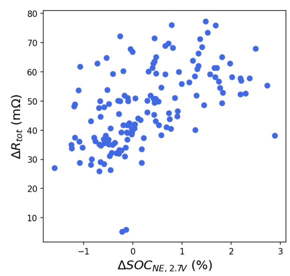

(b)

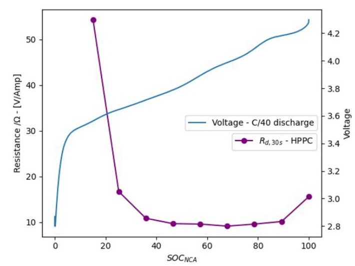

(c)

Fig. S23: **Explaining resistance dependence on SOC. a**) Schematic showing the sign of the shift for more discharged/charged PE/NE. At 2.7V, more discharged NE/PE will display a negative shift. At 4.2V, more charged NE/PE will display a positive shift. **b**) Low SOC ΔR_{tot} plotted as a function of PE and NE SOC shifts at full cell voltage of 2.7V at EOL. As PE gets further discharged resistance increases, but as NE gets further discharged resistance decreases. **c**) Voltage and 30s discharge resistance taken from a NCA/Li pouch cell (see SI Section S.5 for disassembly details). The resistance curve has a bowl shape, where SOC extremes of NCA lead to higher resistance. From these observations we can conclude that the origin of low SOC resistance increase is due to the PE moving to further SOC extremes.

243 ### S.9.3 Further resistance exploration

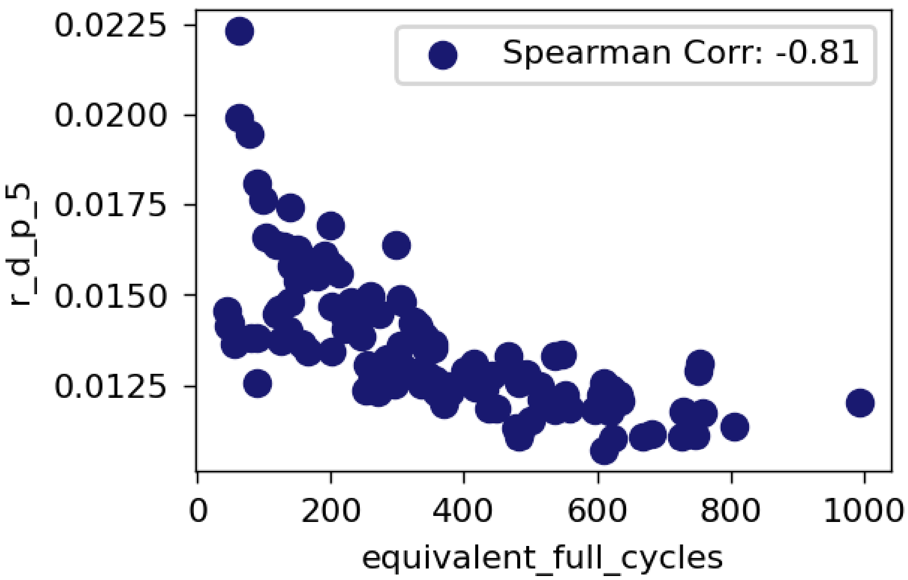

Fig. S24: Strong correlation between R_p at 50% SOC and EFC with a Spearman correlation coefficient of -0.81.

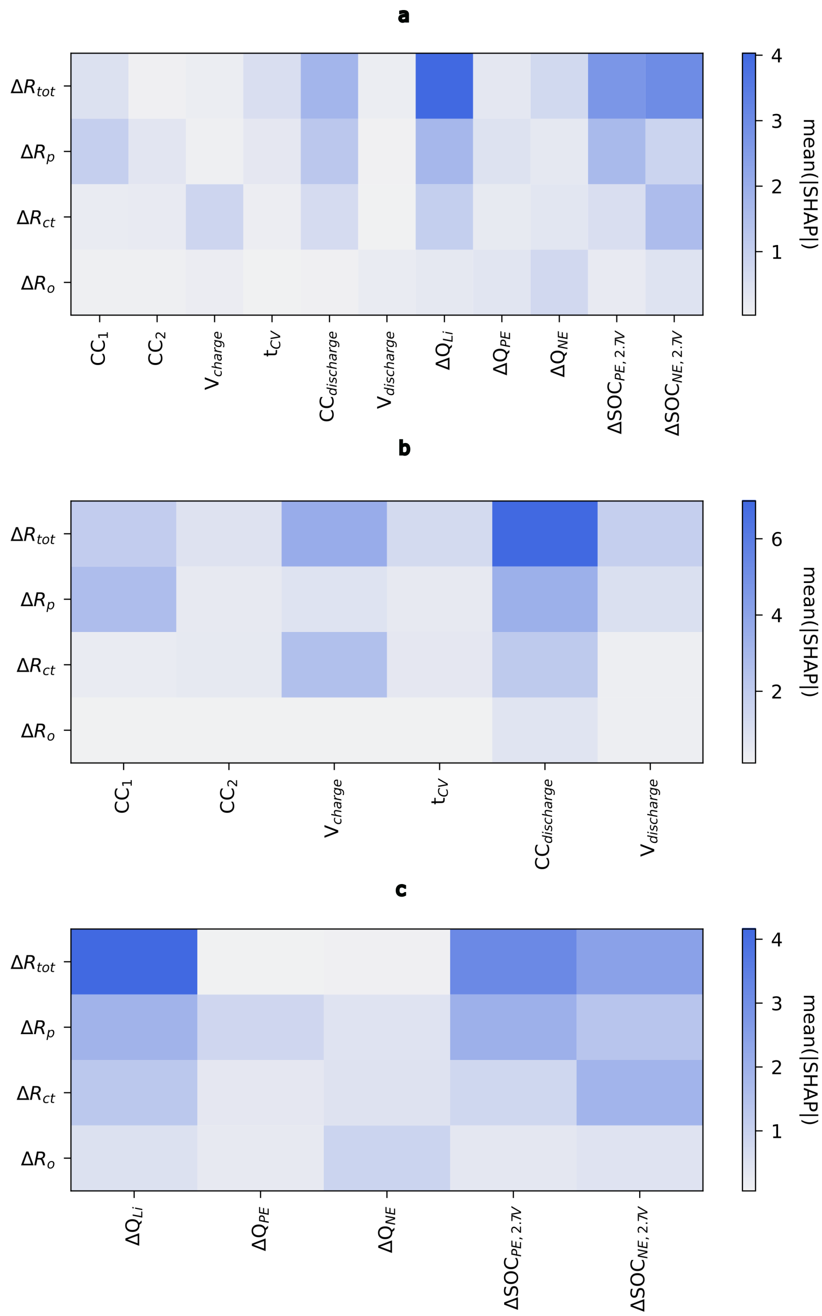

Fig. S25: **Resistance timescale breakdown.** Average mean shap values obtained for different input feature sets for the explanatory model. **a**) Matrix plot built with electrode-specific capacities/SOCs and cycling conditions. **b**) Matrix plot built only with cycling conditions. **c**) Matrix plot built only with electrode-specific capacities/SOCs. By including ΔR_{tot}, ΔR_p, ΔR_{ct}, and ΔR_{ohm} on the same matrix plot we can see how the important features for different timescale resistances come together to make the feature importance ranking for ΔR_{tot}. The resistances predicted here are at 30% SOC.

S.10 Model training and stability

S.10.1 Model training procedures

To ensure the random forest models are robust and do not overfit, we subject the models to a hyperparameter tuning protocol. We first split the dataset in to a train and test set outlined in SI Section S.10.2. The train:test split is roughly 2:1 in size (in practice this is 160 train cells, and 79 test cells). The training set is further split into five equal subsets based on a random seed, four subsets are used for training and the remaining subset is used as a validation set. These subsets are subject to a cross-validation search to find the optimal hyperparameters from the set of hyperparameters in SI Table S6 using *sk-learn GridSearchCV*. Once these hyperparameters are optimized on the train and validation set, they are set and the model is deployed on the test set.

Hyperparameter	**Model input in python sk.learn**	**Parameter range**
Number of Estimators (i.e. Random Forests)	n_estimators	[160, 320, 640]
Minimum Number of Samples to be a Leaf	min_samples_leaf	[1,2,3,4]
Maximum number of features to be considered for each split	max_features	['sqrt', 'log2']
Minimum number of Samples to split a Node	min_samples_split	[2,3,4,5]

Table S6: Range of hyperparameters during Cross Validation Grid Search

S.10.2 Train/test split procedures

When investigating the accuracy of a model, a train-test set split procedure needs to be employed that is representative of the intended application. For example, if the intended use of the model is for quality assurance in cell manufacturing, or R&D optimization for novel operating conditions, then the test set should be designed accordingly [36].

In the design of our model training, we employed an inside-of-domain test scenario, which is schematically depicted in Fig. S26. The inside-of-domain scenario constructs the test set by searching the dataset for cells that have identical cycling protocols. When a cycling protocol has more than 2 repeats, the scenario holds 2 random cells of that protocol in the training set and places the remaining repeats in the test set. As such, the test set will always be comprised of cells that are represented by at least 2 cells in the train set. This is representative of the quality assurance use case where we wish to predict an unseen cell, but previously tested protocols.

An alternative is an out-of-domain test scenario. In this more stringent case, the test set is strictly composed of cells that have a protocol not present in the training set (Fig. S26). In this case, protocols and their subsequent cells would be randomly allocated to either the train set or test set until a certain ratio between cells in the train and test is achieved. This would be representative of a R&D exploration of novel operating conditions use case, and is not analyzed in this study.

The same inside-of-domain train-test split scenario is applied for training all early prediction models for accurate comparison (Fig. 4, Fig 6, Fig. S32). Additionally, the random seed to select the repeated cells going into the train set is fixed across all models shown in this dataset.

In our dataset, this train-test scenario results in roughly a 67/33 train-test split ratio. Despite using the same train-test split scenario, not all models have been trained on exactly the same number of cells.

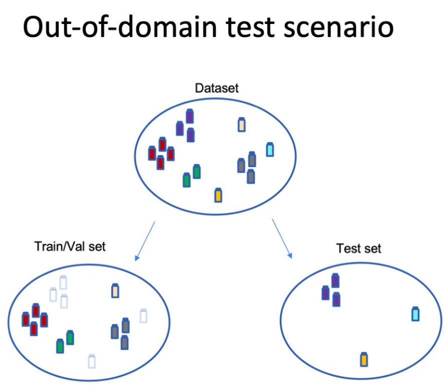

Fig. S26: **Schematic depiction of different testing scenarios.** In our study, we trained models based on the inside-of-domain test scenario. Here we used n=2, for the minimum number of identical cycling protocol cells to be allocated to the train set, before allocating other cells of identical cycling protocol into the test set.

S.10.3 Comparative evaluation between random forest and gradient boosting regressor aging matrices

The aging matrices shown throughout this study have been built on underlying Random Forest models trained on the battery cell's cycling protocol data or early cycling data. The Random forest models have proven to be robust and versatile, as demonstrated in SI Figure S21, with sufficient accuracy, while retaining model interpretability. However, other models including gradient boosting based models, or entirely different model architectures such as neural networks could have been used as the underlying model to run the aging matrix analysis depending on what can best describe the data. For comparison we show that different model choices yields qualitatively similar results when they have similar prediction performance. SI Figure S27 compares the aging matrices constructed from a set of Random Forest models and a set of Gradient Boosting models as the underlying model type. The exact SHAP weights of the specific features vary slightly, but the overall trend and learning are identical.

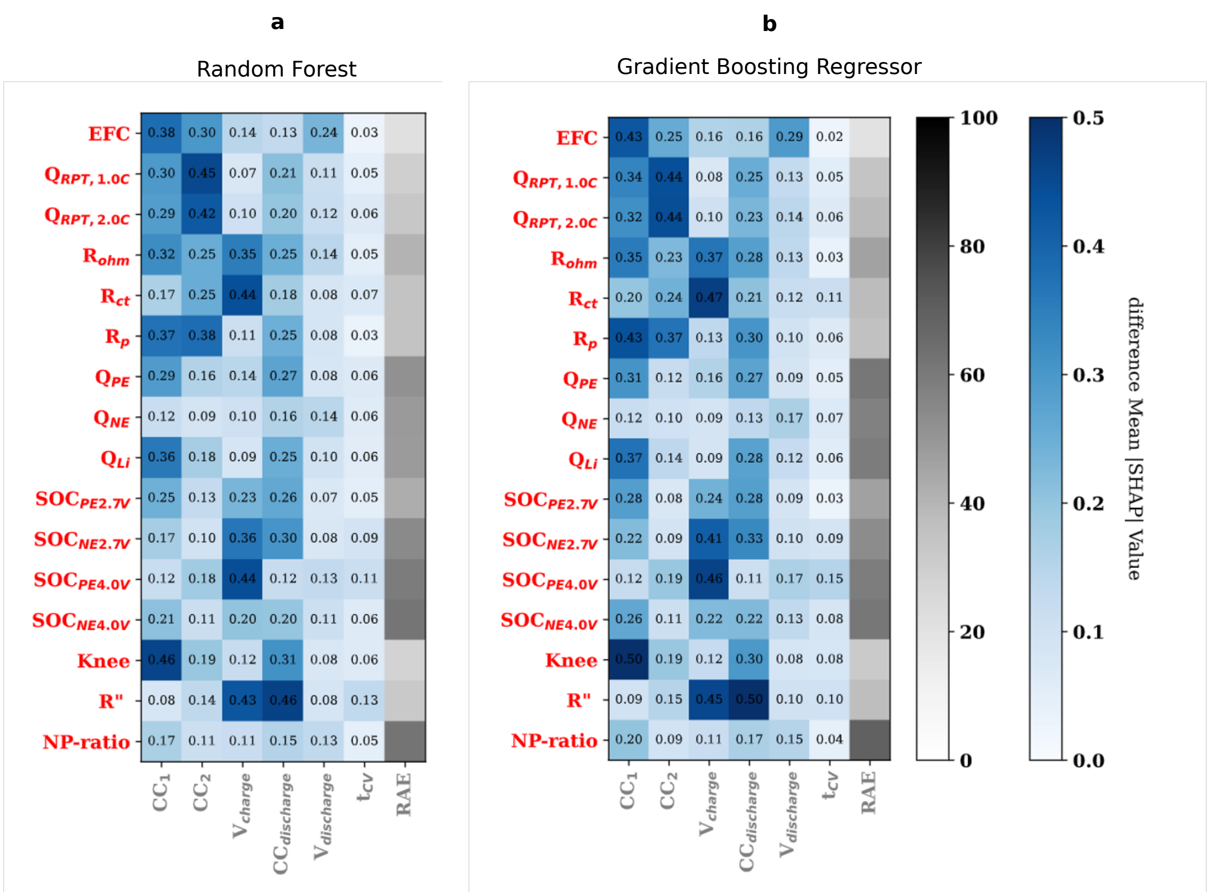

Fig. S27: **Comparative model evaluation between Random Forest and Gradient Boosting Regressor aging matrices**. **a**) Random Forest model-based aging matrix and **b**) Gradient Boosting Regressor model-based aging matrix. These matrices show qualitatively similar feature importances.

S.10.4 Early Prediction Pearson Correlation

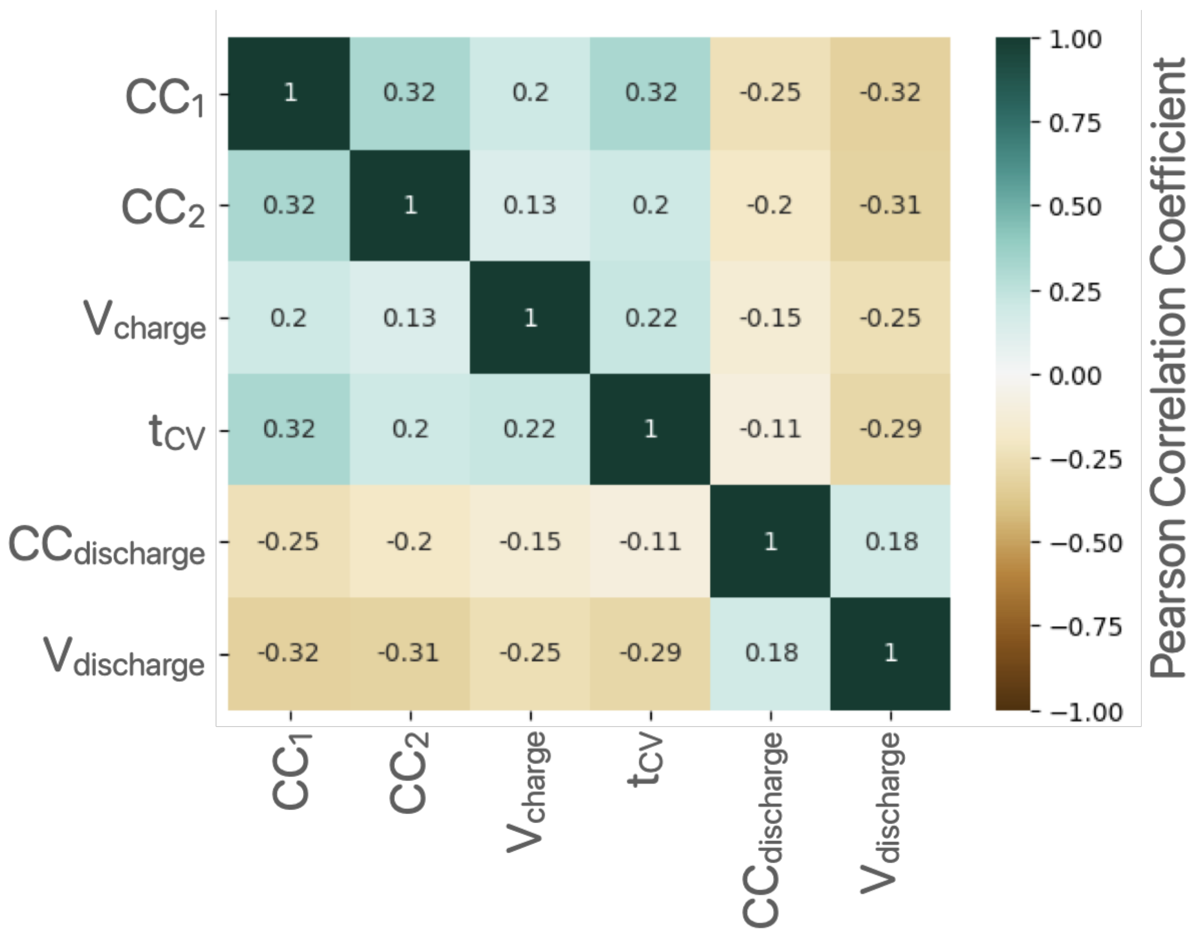

Fig. S28: **Protocol-only model cycling parameter intercorrelation.** The matrix shows the Pearson correlations between aging cycle parameters. The matrix has no high correlations (the maximum magnitude is 0.32) between any of the input parameters varied during the aging cycles. While the random forest regression prediction accuracy should not be significantly negatively affected by feature correlations, highly correlated features can lead the model to report misleading feature importances. This matrix allows us to more comfortably state that the relationships that we identify are not convoluted by strong dependencies between input parameters.

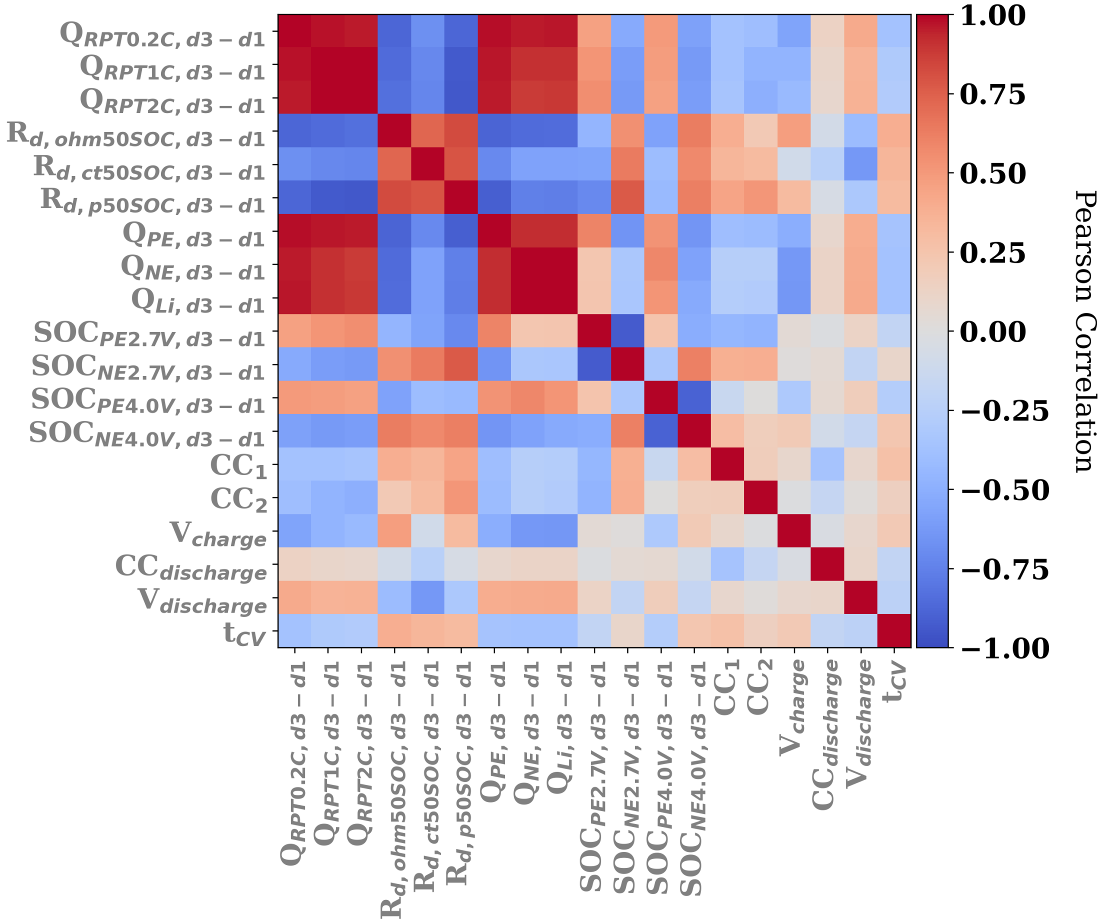

Fig. S29: **Diagnostic-aided model feature intercorrelation.** Model with early mechanistic SOH metrics as inputs as well as cycling conditions. Correlation between all inputs are shown here. We can observe typical trends such as a positive correlation between all three resistance-based features, and a negative correlation between the resistance-based features and the capacity-based features.

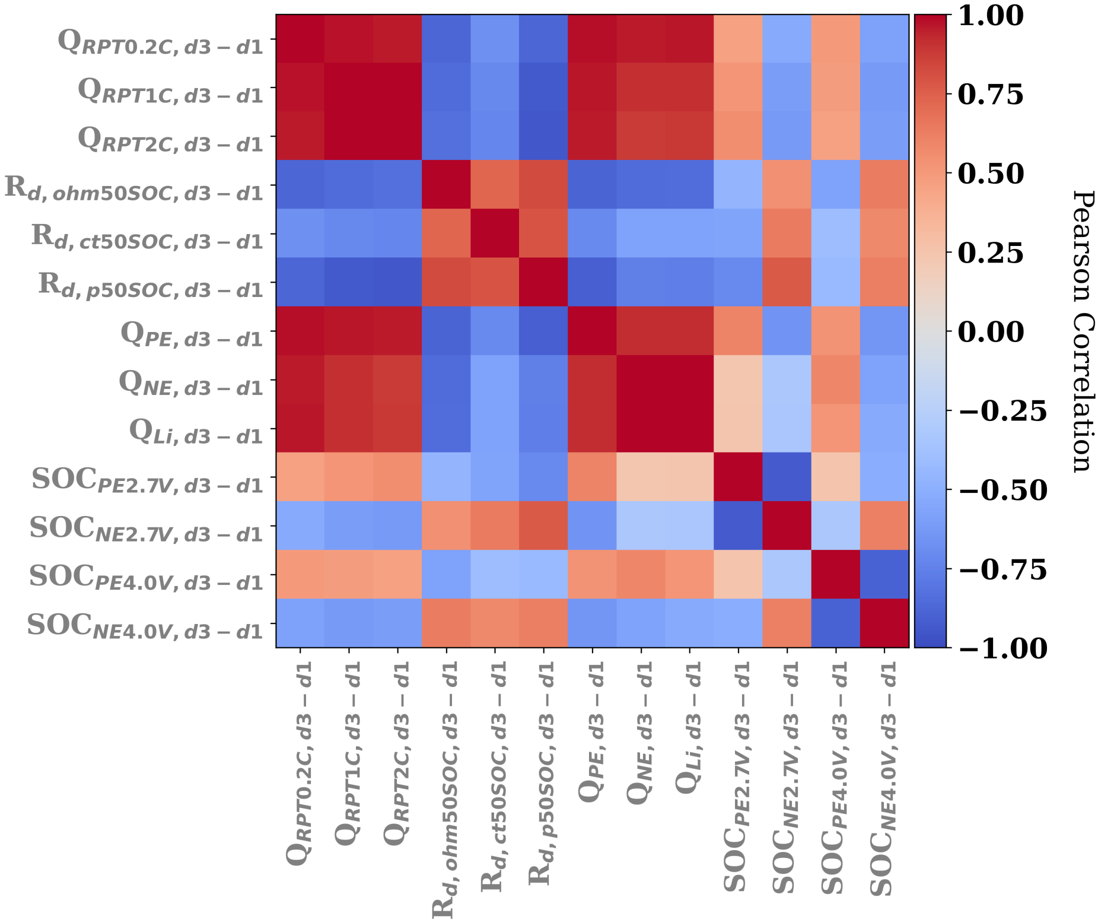

Fig. S30: **Diagnostic-only model feature correlation.** Model with early mechanistic SOH metrics only as inputs. This plot is a subset of the correlations shown in the diagnostic-aided correlation plot (Fig. S29).

S.10.5 Repeat Effect on Matrix Plot

To test the effect of train/test split and retraining models, we generate the aging matrix for the protocol models but choose different random seeds. Three runs are shown in SI Fig. S31 for the protocol model where slight differences in feature importance are observed, but the overall trend is consistent. With this invariance to repetitions, we can confidently say that fixing the train / test seed splits should not affect the qualitative outcomes. For other aging matrices in this work, we adopt the strategy of fixing the train / test seed partition to reduce complexity in the analysis.

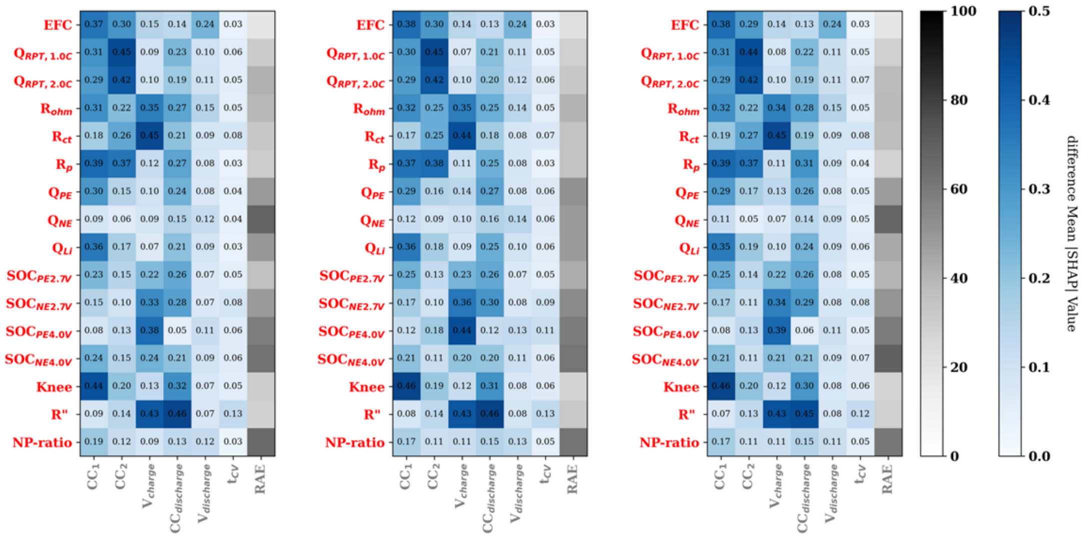

Fig. S31: **Protocol model repeat effect on matrix plot.** Models are retrained with modified train test split partitions and random seed.

S.10.6 Diagnostic-only model

To uncover fundamental relationships between early cycle features and EOL mechanistic SOH metrics, we further developed a "diagnostic-only" model, which does not use cycling parameters as model inputs (SI Fig. S32). This model is important for cases where one is either not interested in the correlations to cycling parameters (to uncover more mechanistic correlations), or cycling parameters are not available. Comparing the diagnostic-aided models to this we are able to deconvolute the relative importance of early mechanistic SOH metrics and cycling conditions (SI Fig. S32). For example, the early prediction of R_{ct} has V_{charge} as the most important feature in the diagnostic-aided model (Fig. 6b) whereas the low and high voltage SOC_{PE} changes are most important for early prediction in the diagnostic-only model (SI Fig. S32). Similarly, in the search of early indicators for the knee indicator the early R_{ct} change is found to be a dominant early predictor only in the absence of the cycling conditions. Although this model should be made in principle to deconvolute early mechanistic SOH metrics and cycling conditions feature importance, the relative order of feature importances does not differ between the "diagnostic-only" model and "diagnostic-aided" models in this case.

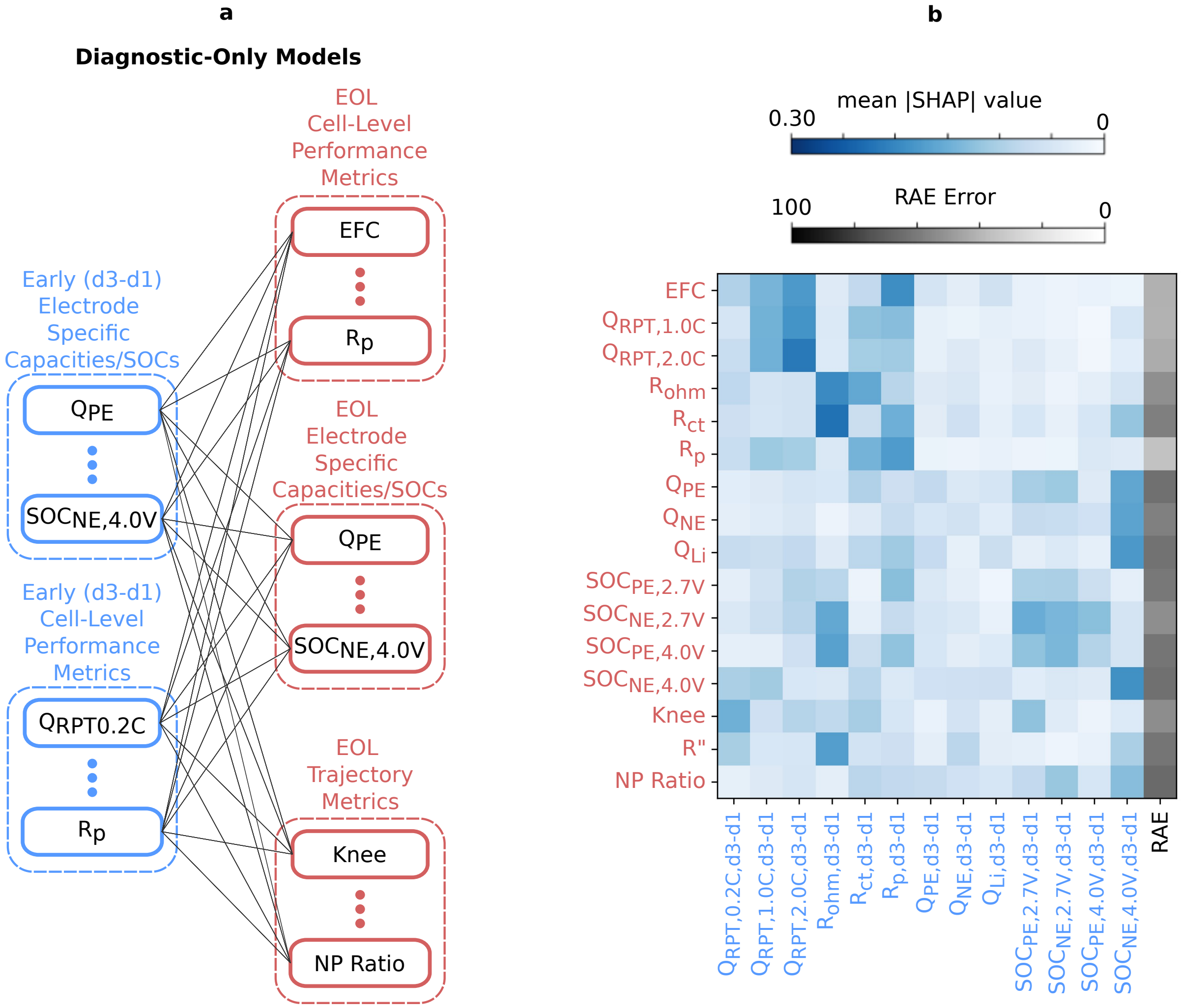

Fig. S32: **Diagnostic-only model. a**) The architecture of the diagnostic-only model with only early mechanistic SOH metrics as inputs. **b**) SHAP analysis degradation matrix showcasing the most important features without the knowledge of cycling conditions. For full parity plots and SHAP plots see SI Section S.10.7.

S.10.7 Parity Plots and SHAP Analysis for All Models

This section shows the parity plots and SHAP analysis for the random forest models that are built for each mechanistic SOH metric for the protocol only, diagnostic aided, and diagnostic only early prediction models. Four error metrics are reported in parity plots, mean absolute percentage error (MAPE), mean absolute error (MAE), relative absolute error (RAE), and the R-squared (R2). MAPE and MAE metrics are less useful when comparing different models due to the difference in prediction scales. Instead RAE and R2 can be used to compare different models with RAE being the error metric chosen to present on the matrix plots. Errors are reported for both the train set and the test set (see SI Section S26 for train/test split).

319 # Protocol Only Models

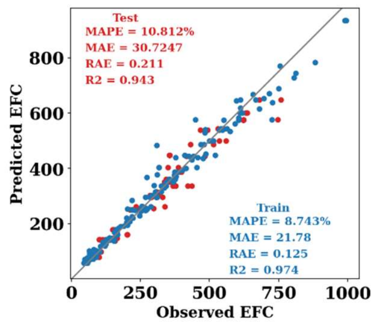

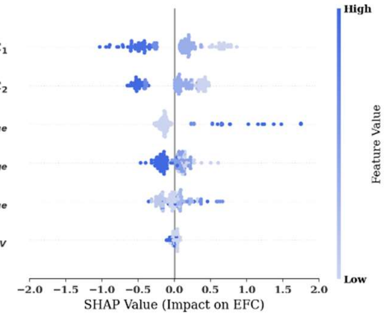

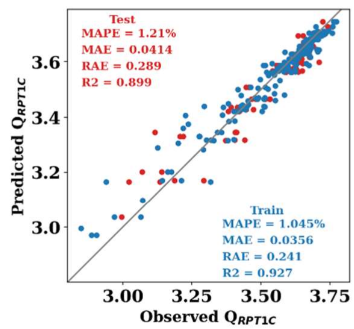

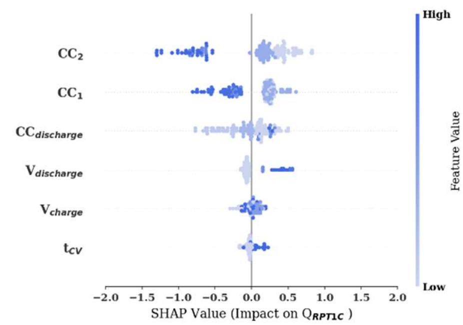

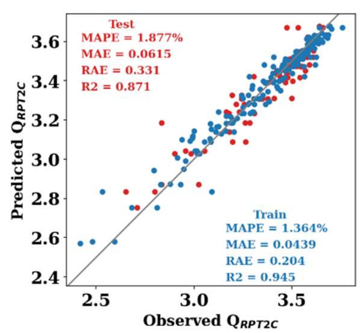

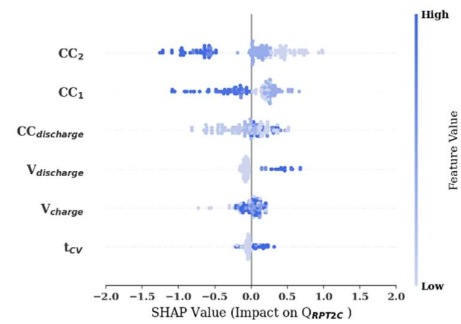

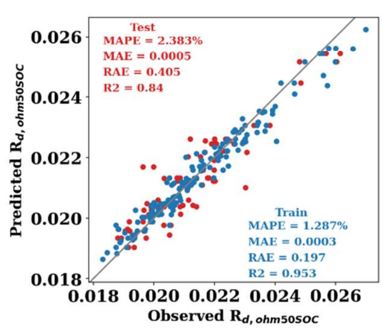

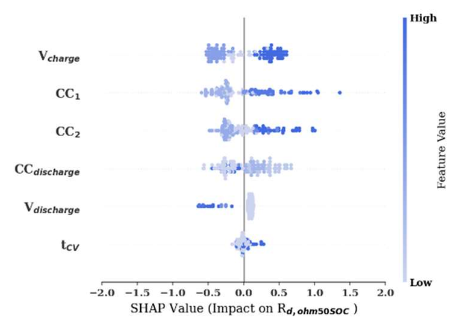

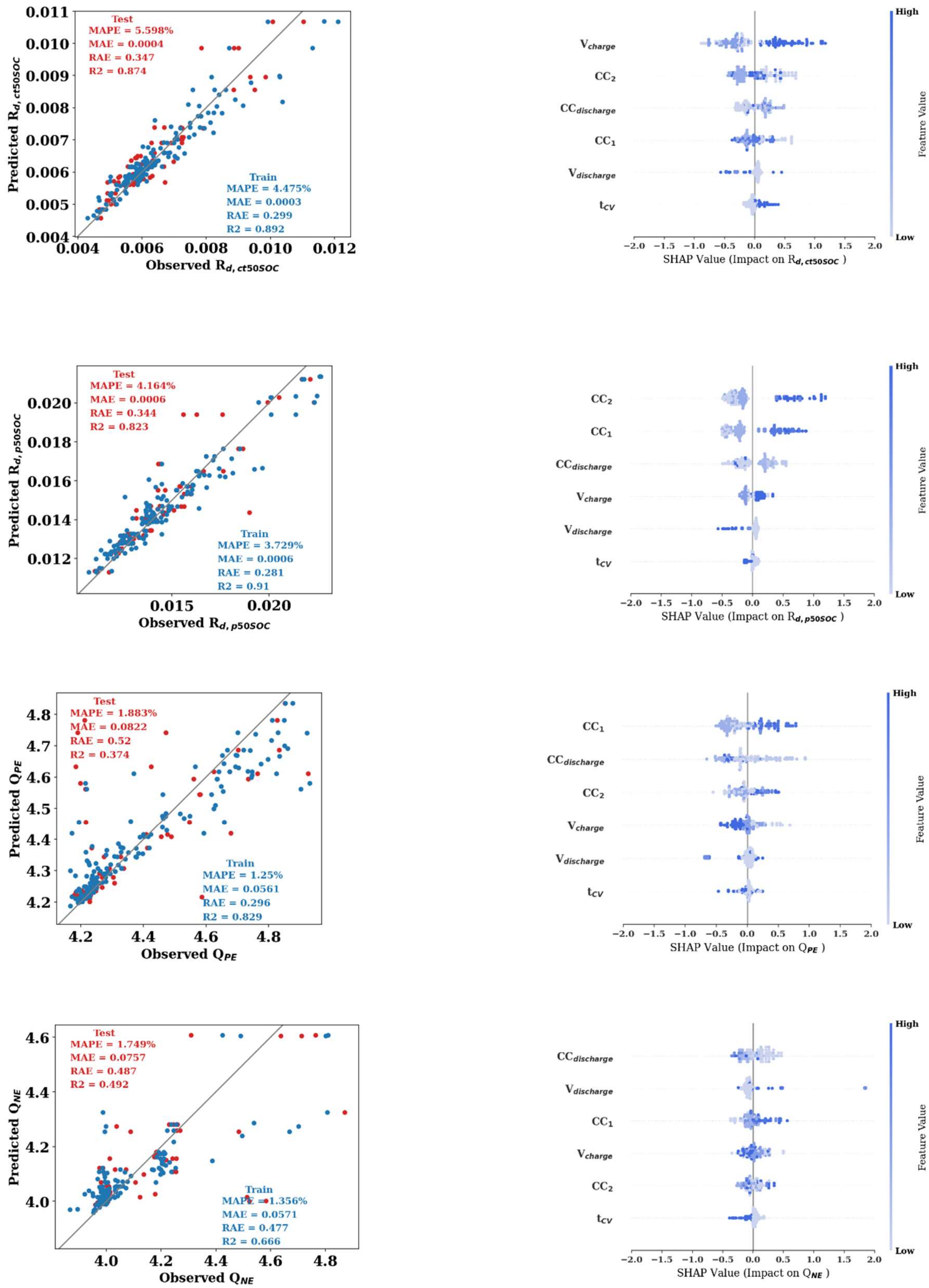

Test
MAPE = 5.598%
MAE = 0.0004
RAE = 0.347
R2 = 0.874
Train
MAPE = 4.475%
MAE = 0.0003
RAE = 0.299
R2 = 0.892
Predicted R$_{d,ct50SOC}$
Observed R$_{d,ct50SOC}$
V$_{charge}$
CC$_2$
CC$_{discharge}$
CC$_1$
V$_{discharge}$
t$_{CV}$
SHAP Value (Impact on R$_{d,ct50SOC}$)
High
Low
Feature Value
Test
MAPE = 4.164%
MAE = 0.0006
RAE = 0.344
R2 = 0.823
Train
MAPE = 3.729%
MAE = 0.0006
RAE = 0.281
R2 = 0.91
Predicted R$_{d,p50SOC}$
Observed R$_{d,p50SOC}$
SHAP Value (Impact on R$_{d,p50SOC}$)
Test
MAPE = 1.883%
MAE = 0.0822
RAE = 0.52
R2 = 0.374
Train
MAPE = 1.25%
MAE = 0.0561
RAE = 0.296
R2 = 0.829
Predicted Q$_{PE}$
Observed Q$_{PE}$
SHAP Value (Impact on Q$_{PE}$)
Test
MAPE = 1.749%
MAE = 0.0757
RAE = 0.487
R2 = 0.492
Train
MAPE = 1.356%
MAE = 0.0571
RAE = 0.477
R2 = 0.666
Predicted Q$_{NE}$
Observed Q$_{NE}$
SHAP Value (Impact on Q$_{NE}$)

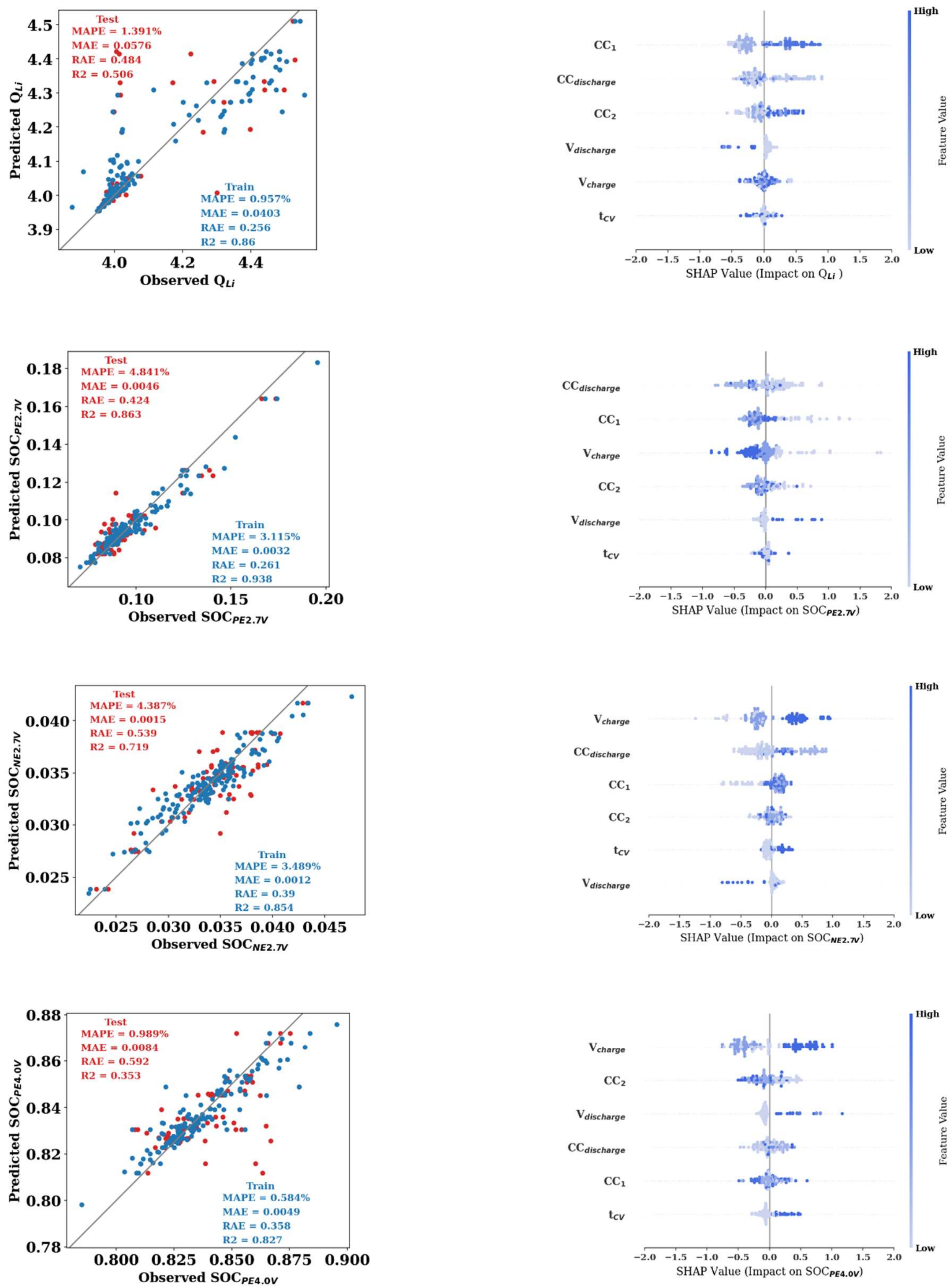
Test
MAPE = 1.391%
MAE = 0.0576
RAE = 0.484
R2 = 0.506
Train
MAPE = 0.957%
MAE = 0.0403
RAE = 0.256
R2 = 0.86
Predicted Q_Li
Observed Q_Li
CC_1
CC_discharge
CC_2
V_discharge
V_charge
t_CV
SHAP Value (Impact on Q_Li)
Feature Value
High
Low
Test
MAPE = 4.841%
MAE = 0.0046
RAE = 0.424
R2 = 0.863
Train
MAPE = 3.115%
MAE = 0.0032
RAE = 0.261
R2 = 0.938
Predicted SOC_PE2.7V
Observed SOC_PE2.7V
SHAP Value (Impact on SOC_PE2.7V)
Test
MAPE = 4.387%
MAE = 0.0015
RAE = 0.539
R2 = 0.719
Train
MAPE = 3.489%
MAE = 0.0012
RAE = 0.39
R2 = 0.854
Predicted SOC_NE2.7V
Observed SOC_NE2.7V
SHAP Value (Impact on SOC_NE2.7V)
Test
MAPE = 0.989%
MAE = 0.0084
RAE = 0.592
R2 = 0.353
Train
MAPE = 0.584%
MAE = 0.0049
RAE = 0.358
R2 = 0.827
Predicted SOC_PE4.0V
Observed SOC_PE4.0V
SHAP Value (Impact on SOC_PE4.0V)

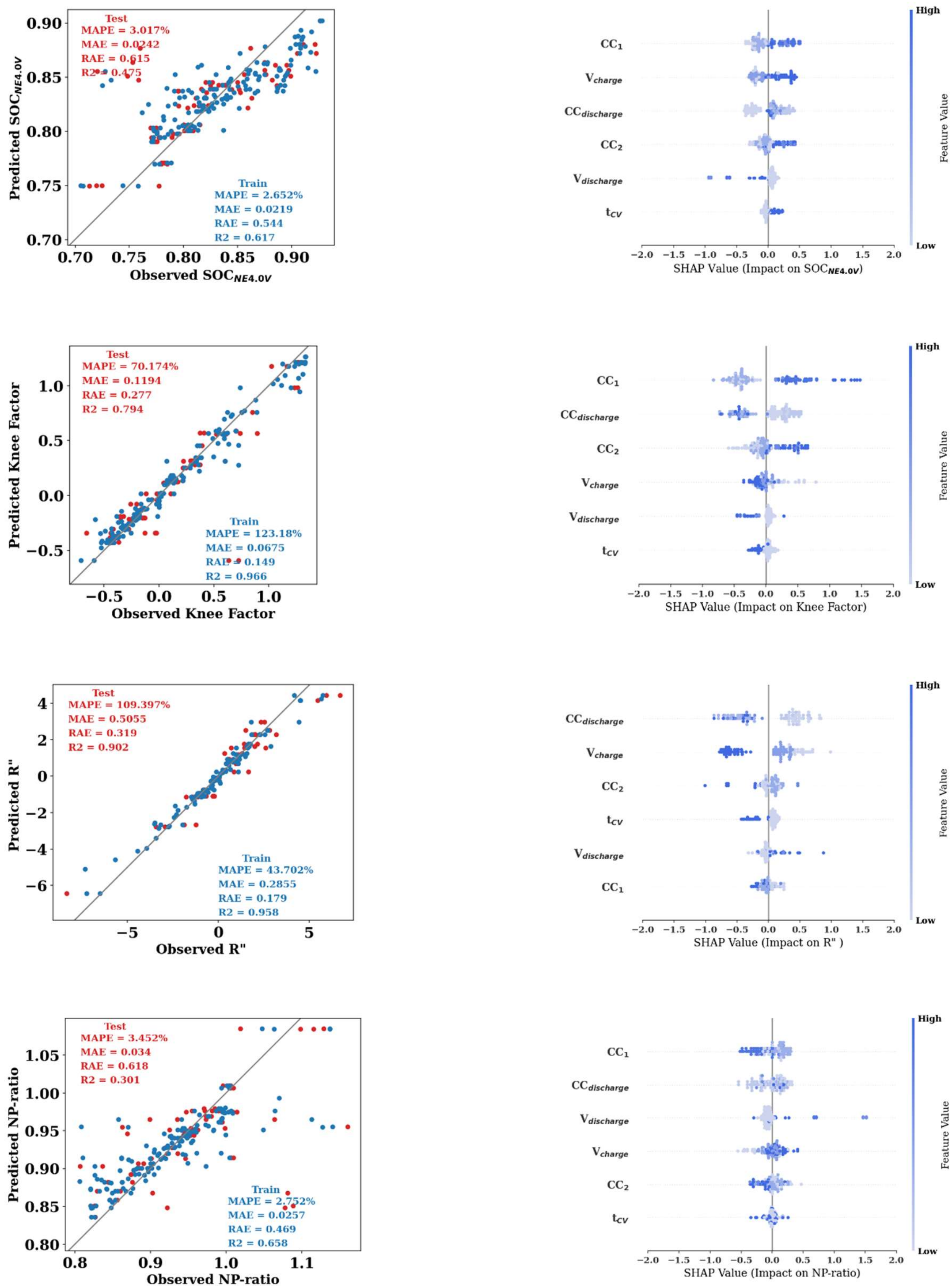

Diagnostic-Only Models

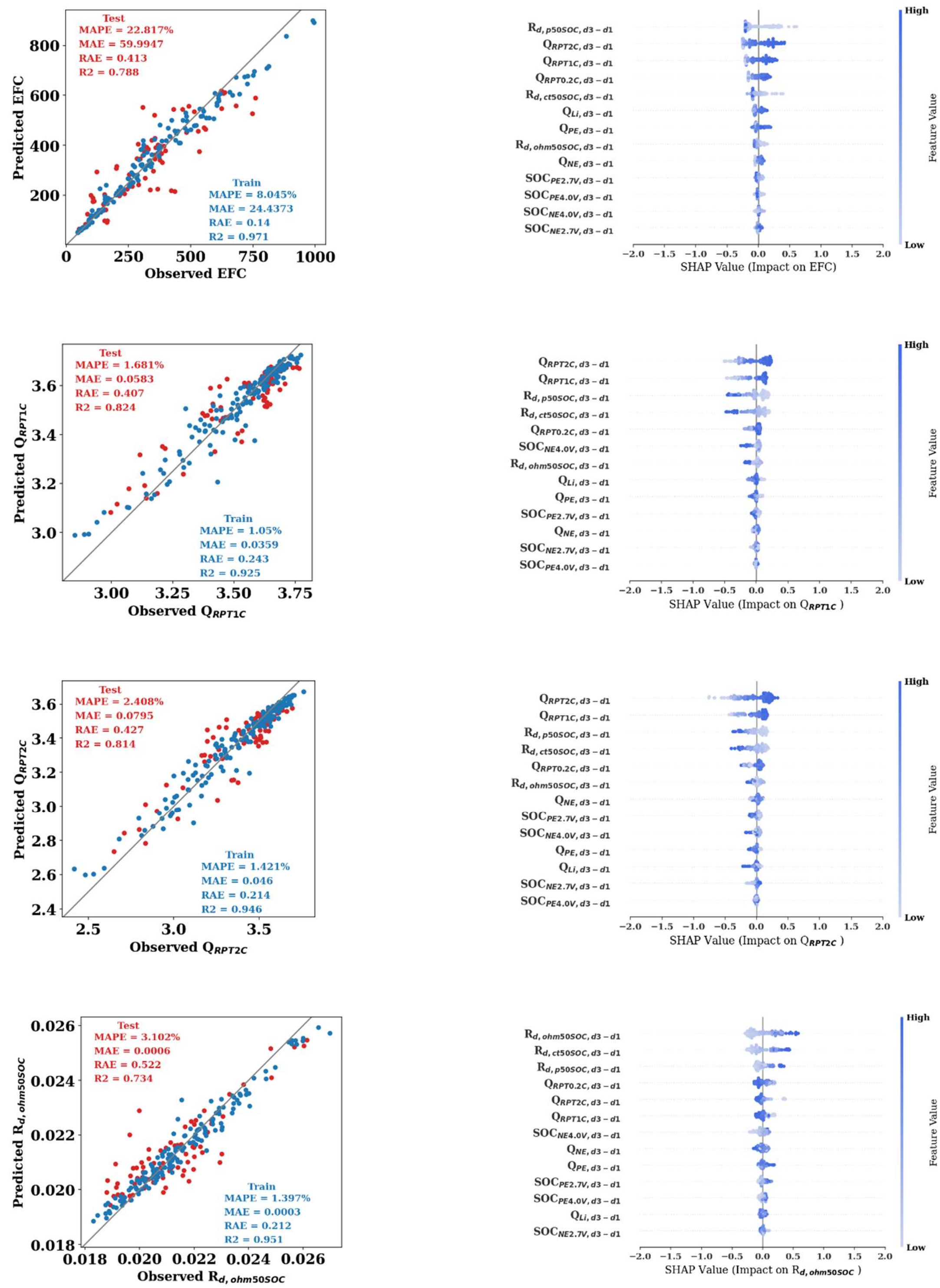
Test
MAPE = 22.817%
MAE = 59.9947
RAE = 0.413
R2 = 0.788
Train
MAPE = 8.045%
MAE = 24.4373
RAE = 0.14
R2 = 0.971
Predicted EFC
Observed EFC
SHAP Value (Impact on EFC)
Feature Value
High
Low
Test
MAPE = 1.681%
MAE = 0.0583
RAE = 0.407
R2 = 0.824
Train
MAPE = 1.05%
MAE = 0.0359
RAE = 0.243
R2 = 0.925
Predicted Q_{RPT1C}
Observed Q_{RPT1C}
SHAP Value (Impact on Q_{RPT1C})
Test
MAPE = 2.408%
MAE = 0.0795
RAE = 0.427
R2 = 0.814
Train
MAPE = 1.421%
MAE = 0.046
RAE = 0.214
R2 = 0.946
Predicted Q_{RPT2C}
Observed Q_{RPT2C}
SHAP Value (Impact on Q_{RPT2C})
Test
MAPE = 3.102%
MAE = 0.0006
RAE = 0.522
R2 = 0.734
Train
MAPE = 1.397%
MAE = 0.0003
RAE = 0.212
R2 = 0.951
Predicted $R_{d,ohm50SOC}$
Observed $R_{d,ohm50SOC}$
SHAP Value (Impact on $R_{d,ohm50SOC}$)

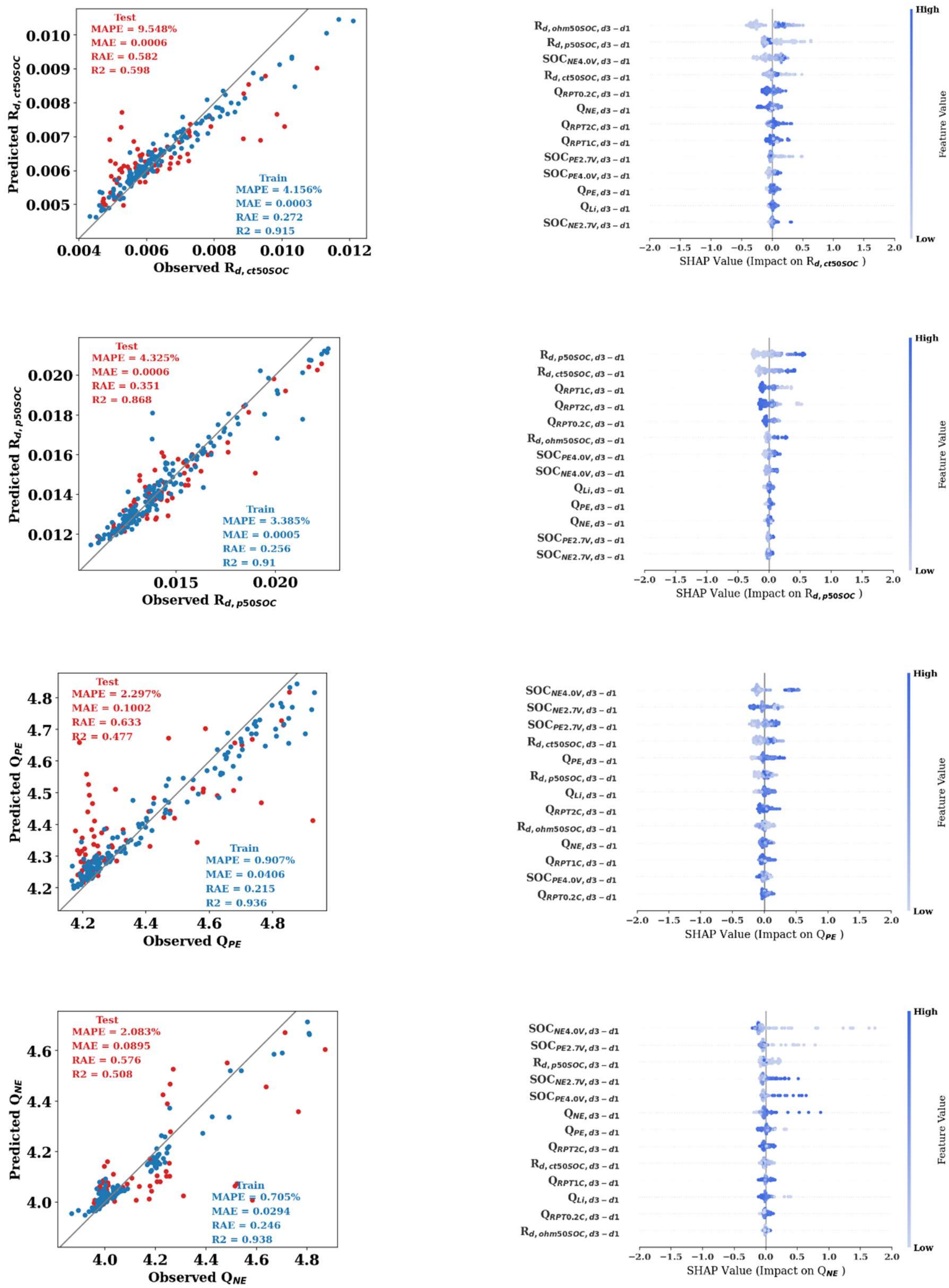
Test
MAPE = 9.548%
MAE = 0.0006
RAE = 0.582
R2 = 0.598
Train
MAPE = 4.156%
MAE = 0.0003
RAE = 0.272
R2 = 0.915
Predicted $R_{d,ct50SOC}$
Observed $R_{d,ct50SOC}$
SHAP Value (Impact on $R_{d,ct50SOC}$)
Test
MAPE = 4.325%
MAE = 0.0006
RAE = 0.351
R2 = 0.868
Train
MAPE = 3.385%
MAE = 0.0005
RAE = 0.256
R2 = 0.91
Predicted $R_{d,p50SOC}$
Observed $R_{d,p50SOC}$
SHAP Value (Impact on $R_{d,p50SOC}$)
Test
MAPE = 2.297%
MAE = 0.1002
RAE = 0.633
R2 = 0.477
Train
MAPE = 0.907%
MAE = 0.0406
RAE = 0.215
R2 = 0.936
Predicted Q_{PE}
Observed Q_{PE}
SHAP Value (Impact on Q_{PE})
Test
MAPE = 2.083%
MAE = 0.0895
RAE = 0.576
R2 = 0.508
Train
MAPE = 0.705%
MAE = 0.0294
RAE = 0.246
R2 = 0.938
Predicted Q_{NE}
Observed Q_{NE}
SHAP Value (Impact on Q_{NE})
High
Low
Feature Value

325

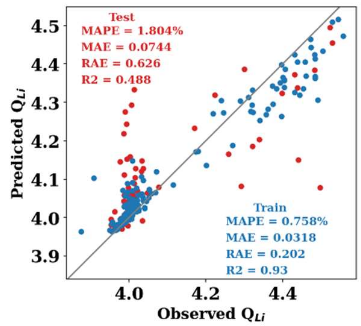

Test
MAPE = 1.804%
MAE = 0.0744
RAE = 0.626
R2 = 0.488
Train
MAPE = 0.758%
MAE = 0.0318
RAE = 0.202
R2 = 0.93
Predicted Q_{Li}
Observed Q_{Li}

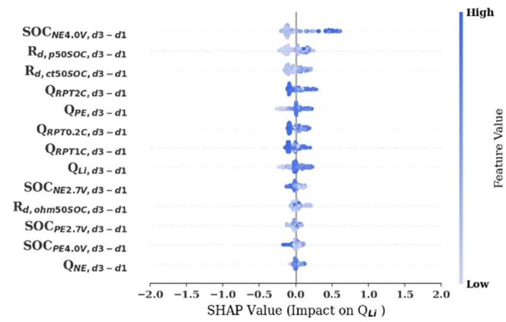

High
Low
Feature Value
SHAP Value (Impact on Q_{Li})

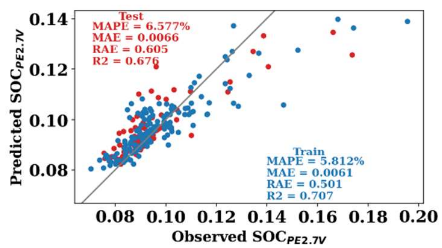

Test
MAPE = 6.577%
MAE = 0.0066
RAE = 0.605
R2 = 0.676
Train
MAPE = 5.812%
MAE = 0.0061
RAE = 0.501
R2 = 0.707
Predicted $SOC_{PE2.7V}$
Observed $SOC_{PE2.7V}$

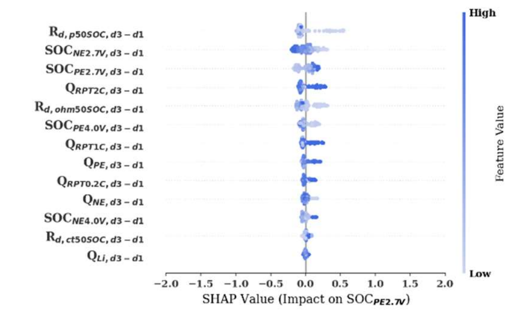

High
Low
Feature Value
SHAP Value (Impact on $SOC_{PE2.7V}$)

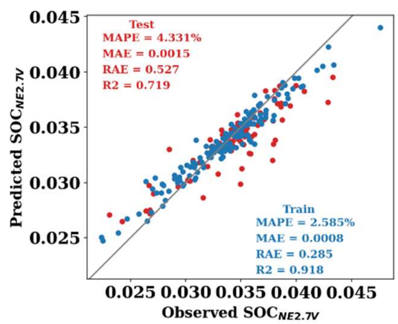

Test
MAPE = 4.331%
MAE = 0.0015
RAE = 0.527
R2 = 0.719
Train
MAPE = 2.585%
MAE = 0.0008
RAE = 0.285
R2 = 0.918
Predicted $SOC_{NE2.7V}$
Observed $SOC_{NE2.7V}$

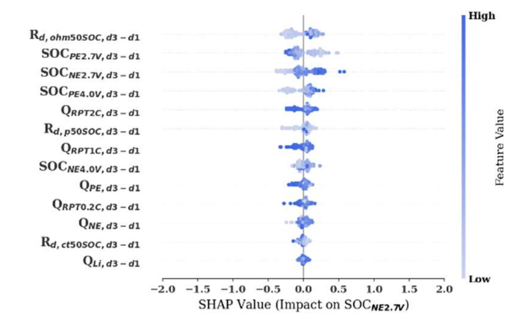

High
Low
Feature Value
SHAP Value (Impact on $SOC_{NE2.7V}$)

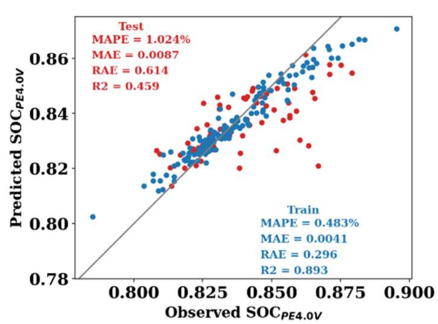

Test
MAPE = 1.024%
MAE = 0.0087
RAE = 0.614
R2 = 0.459
Train
MAPE = 0.483%
MAE = 0.0041
RAE = 0.296
R2 = 0.893
Predicted $SOC_{PE4.0V}$
Observed $SOC_{PE4.0V}$

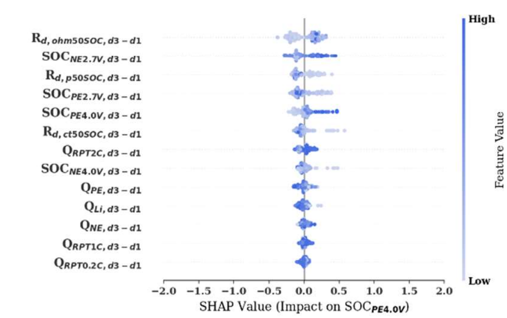

High
Low
Feature Value
SHAP Value (Impact on $SOC_{PE4.0V}$)

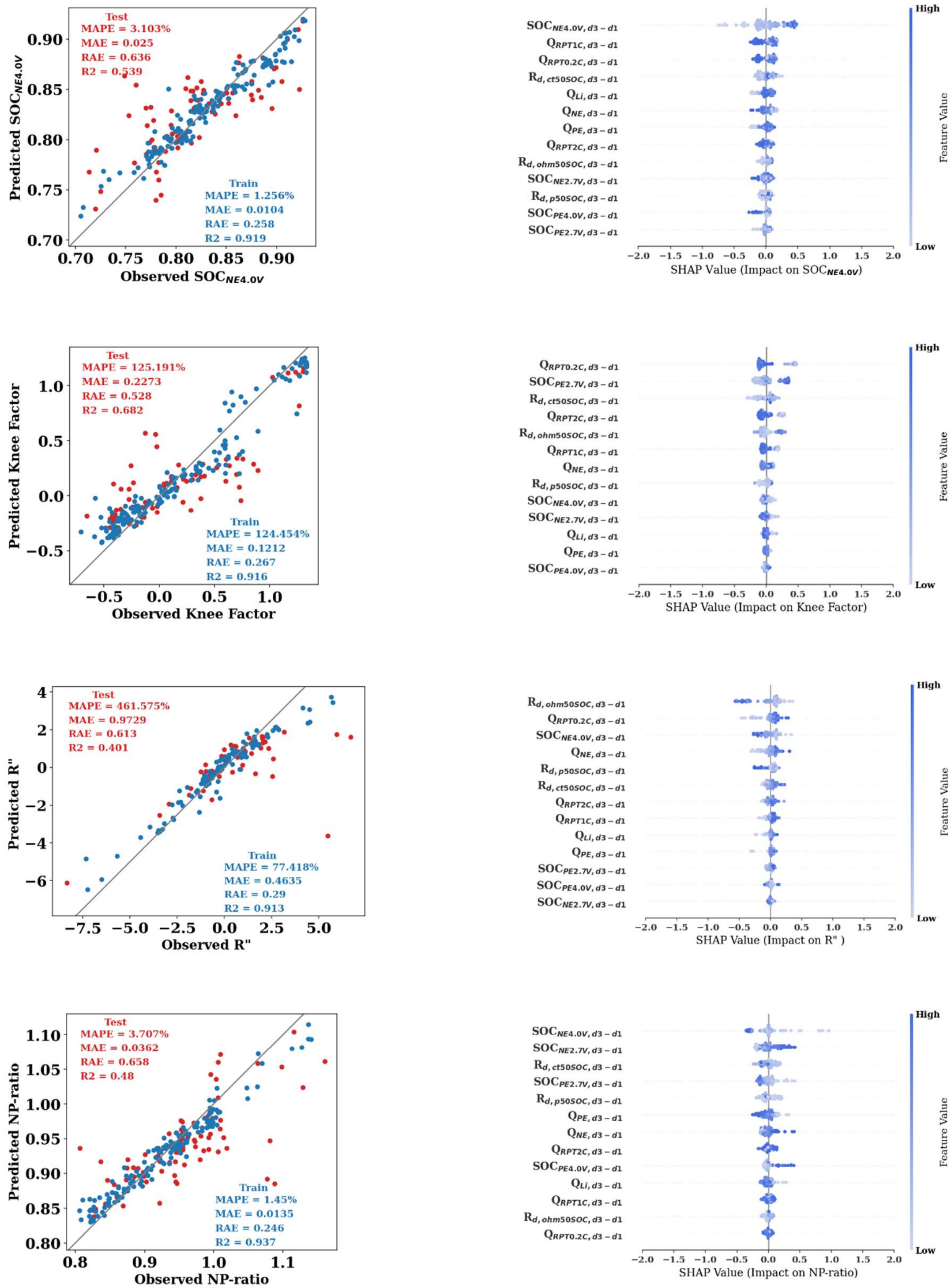

Diagnostic-Aided Models

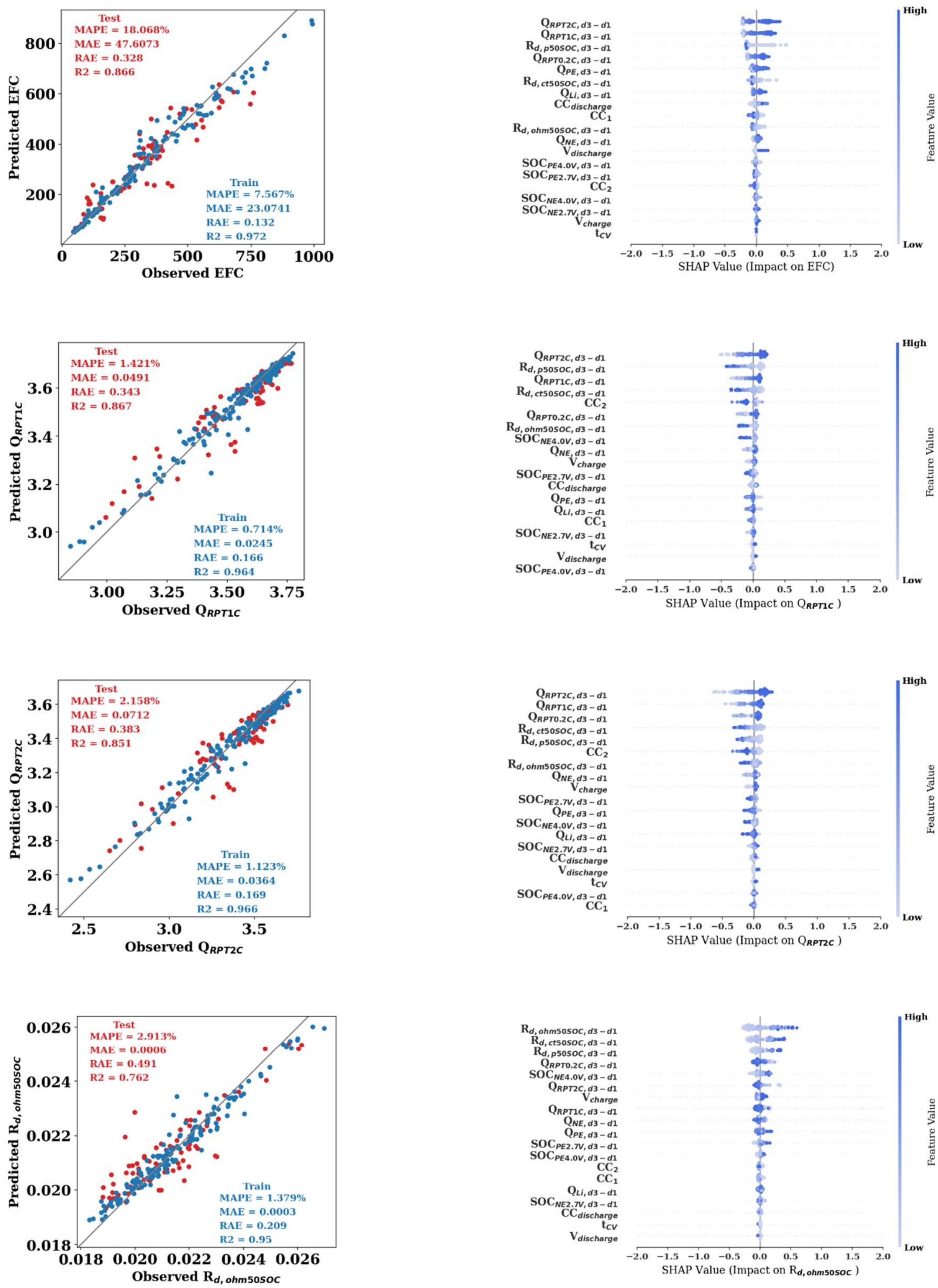

Test
MAPE = 18.068%
MAE = 47.6073
RAE = 0.328
R2 = 0.866
Train
MAPE = 7.567%
MAE = 23.0741
RAE = 0.132
R2 = 0.972
Predicted EFC
Observed EFC
800
600
400
200
0
250
500
750
1000
$Q_{RPT2C,d3-d1}$
$Q_{RPT1C,d3-d1}$
$R_{d,p50SOC,d3-d1}$
$Q_{RPT0.2C,d3-d1}$
$Q_{PE,d3-d1}$
$R_{d,ct50SOC,d3-d1}$
$Q_{Li,d3-d1}$
$CC_{discharge}$
CC_1
$R_{d,ohm50SOC,d3-d1}$
$Q_{NE,d3-d1}$
$V_{discharge}$
$SOC_{PE4.0V,d3-d1}$
$SOC_{PE2.7V,d3-d1}$
CC_2
$SOC_{NE4.0V,d3-d1}$
$SOC_{NE2.7V,d3-d1}$
V_{charge}
t_{CV}
SHAP Value (Impact on EFC)
High
Feature Value
Low
Test
MAPE = 1.421%
MAE = 0.0491
RAE = 0.343
R2 = 0.867
Train
MAPE = 0.714%
MAE = 0.0245
RAE = 0.166
R2 = 0.964
Predicted Q_{RPT1C}
Observed Q_{RPT1C}
3.6
3.4
3.2
3.0
3.00
3.25
3.50
3.75
$Q_{RPT2C,d3-d1}$
$R_{d,p50SOC,d3-d1}$
$Q_{RPT1C,d3-d1}$
$R_{d,ct50SOC,d3-d1}$
CC_2
$Q_{RPT0.2C,d3-d1}$
$R_{d,ohm50SOC,d3-d1}$
$SOC_{NE4.0V,d3-d1}$
$Q_{NE,d3-d1}$
V_{charge}
$SOC_{PE2.7V,d3-d1}$
$CC_{discharge}$
$Q_{PE,d3-d1}$
$Q_{Li,d3-d1}$
CC_1
$SOC_{NE2.7V,d3-d1}$
t_{CV}
$V_{discharge}$
$SOC_{PE4.0V,d3-d1}$
SHAP Value (Impact on Q_{RPT1C})
High
Feature Value
Low
Test
MAPE = 2.158%
MAE = 0.0712
RAE = 0.383
R2 = 0.851
Train
MAPE = 1.123%
MAE = 0.0364
RAE = 0.169
R2 = 0.966
Predicted Q_{RPT2C}
Observed Q_{RPT2C}
3.6
3.4
3.2
3.0
2.8
2.6
2.4
2.5
3.0
3.5
$Q_{RPT2C,d3-d1}$
$Q_{RPT1C,d3-d1}$
$Q_{RPT0.2C,d3-d1}$
$R_{d,ct50SOC,d3-d1}$
$R_{d,p50SOC,d3-d1}$
CC_2
$R_{d,ohm50SOC,d3-d1}$
$Q_{NE,d3-d1}$
V_{charge}
$SOC_{PE2.7V,d3-d1}$
$Q_{PE,d3-d1}$
$SOC_{NE4.0V,d3-d1}$
$Q_{Li,d3-d1}$
$SOC_{NE2.7V,d3-d1}$
$CC_{discharge}$
$V_{discharge}$
t_{CV}
$SOC_{PE4.0V,d3-d1}$
CC_1
SHAP Value (Impact on Q_{RPT2C})
High
Feature Value
Low
Test
MAPE = 2.913%
MAE = 0.0006
RAE = 0.491
R2 = 0.762
Train
MAPE = 1.379%
MAE = 0.0003
RAE = 0.209
R2 = 0.95
Predicted $R_{d,ohm50SOC}$
Observed $R_{d,ohm50SOC}$
0.026
0.024
0.022
0.020
0.018
$R_{d,ohm50SOC,d3-d1}$
$R_{d,ct50SOC,d3-d1}$
$R_{d,p50SOC,d3-d1}$
$Q_{RPT0.2C,d3-d1}$
$SOC_{NE4.0V,d3-d1}$
$Q_{RPT2C,d3-d1}$
V_{charge}
$Q_{RPT1C,d3-d1}$
$Q_{NE,d3-d1}$
$Q_{PE,d3-d1}$
$SOC_{PE2.7V,d3-d1}$
$SOC_{PE4.0V,d3-d1}$
CC_2
CC_1
$Q_{Li,d3-d1}$
$SOC_{NE2.7V,d3-d1}$
$CC_{discharge}$
t_{CV}
$V_{discharge}$
SHAP Value (Impact on $R_{d,ohm50SOC}$)
High
Feature Value
Low
−2.0
−1.5
−1.0
−0.5
0.0
0.5
1.0
1.5
2.0

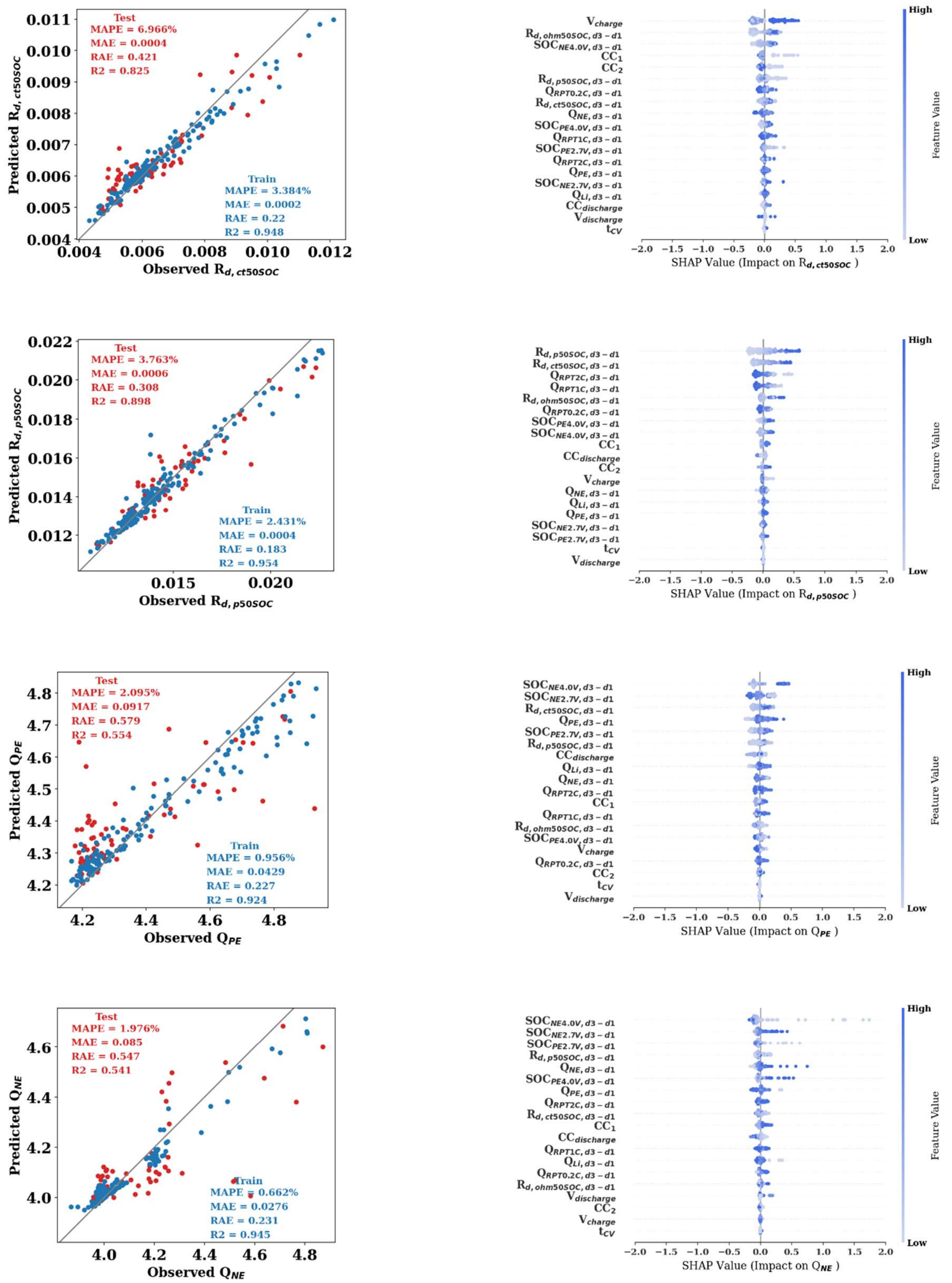
Test
MAPE = 6.966%
MAE = 0.0004
RAE = 0.421
R2 = 0.825
Train
MAPE = 3.384%
MAE = 0.0002
RAE = 0.22
R2 = 0.948
Predicted $R_{d,ct50SOC}$
Observed $R_{d,ct50SOC}$
SHAP Value (Impact on $R_{d,ct50SOC}$)
Test
MAPE = 3.763%
MAE = 0.0006
RAE = 0.308
R2 = 0.898
Train
MAPE = 2.431%
MAE = 0.0004
RAE = 0.183
R2 = 0.954
Predicted $R_{d,p50SOC}$
Observed $R_{d,p50SOC}$
SHAP Value (Impact on $R_{d,p50SOC}$)
Test
MAPE = 2.095%
MAE = 0.0917
RAE = 0.579
R2 = 0.554
Train
MAPE = 0.956%
MAE = 0.0429
RAE = 0.227
R2 = 0.924
Predicted Q_{PE}
Observed Q_{PE}
SHAP Value (Impact on Q_{PE})
Test
MAPE = 1.976%
MAE = 0.085
RAE = 0.547
R2 = 0.541
Train
MAPE = 0.662%
MAE = 0.0276
RAE = 0.231
R2 = 0.945
Predicted Q_{NE}
Observed Q_{NE}
SHAP Value (Impact on Q_{NE})
High
Low
Feature Value

329

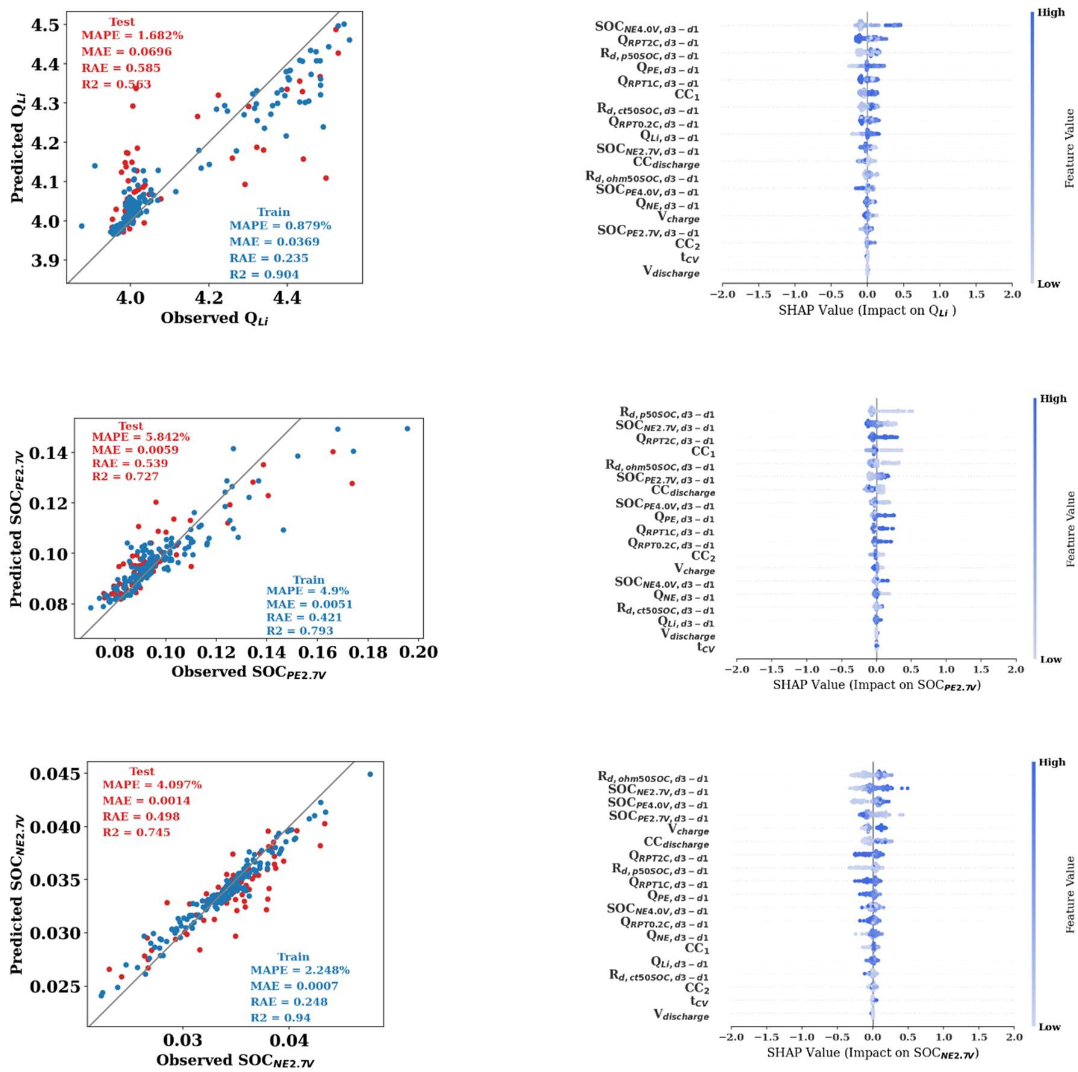

Test
MAPE = 1.682%
MAE = 0.0696
RAE = 0.585
R2 = 0.563
Train
MAPE = 0.879%
MAE = 0.0369
RAE = 0.235
R2 = 0.904
Predicted Q_{Li}
Observed Q_{Li}
SHAP Value (Impact on Q_{Li})
Feature Value
High
Low
Test
MAPE = 5.842%
MAE = 0.0059
RAE = 0.539
R2 = 0.727
Train
MAPE = 4.9%
MAE = 0.0051
RAE = 0.421
R2 = 0.793
Predicted $SOC_{PE2.7V}$
Observed $SOC_{PE2.7V}$
SHAP Value (Impact on $SOC_{PE2.7V}$)
Test
MAPE = 4.097%
MAE = 0.0014
RAE = 0.498
R2 = 0.745
Train
MAPE = 2.248%
MAE = 0.0007
RAE = 0.248
R2 = 0.94
Predicted $SOC_{NE2.7V}$
Observed $SOC_{NE2.7V}$
SHAP Value (Impact on $SOC_{NE2.7V}$)

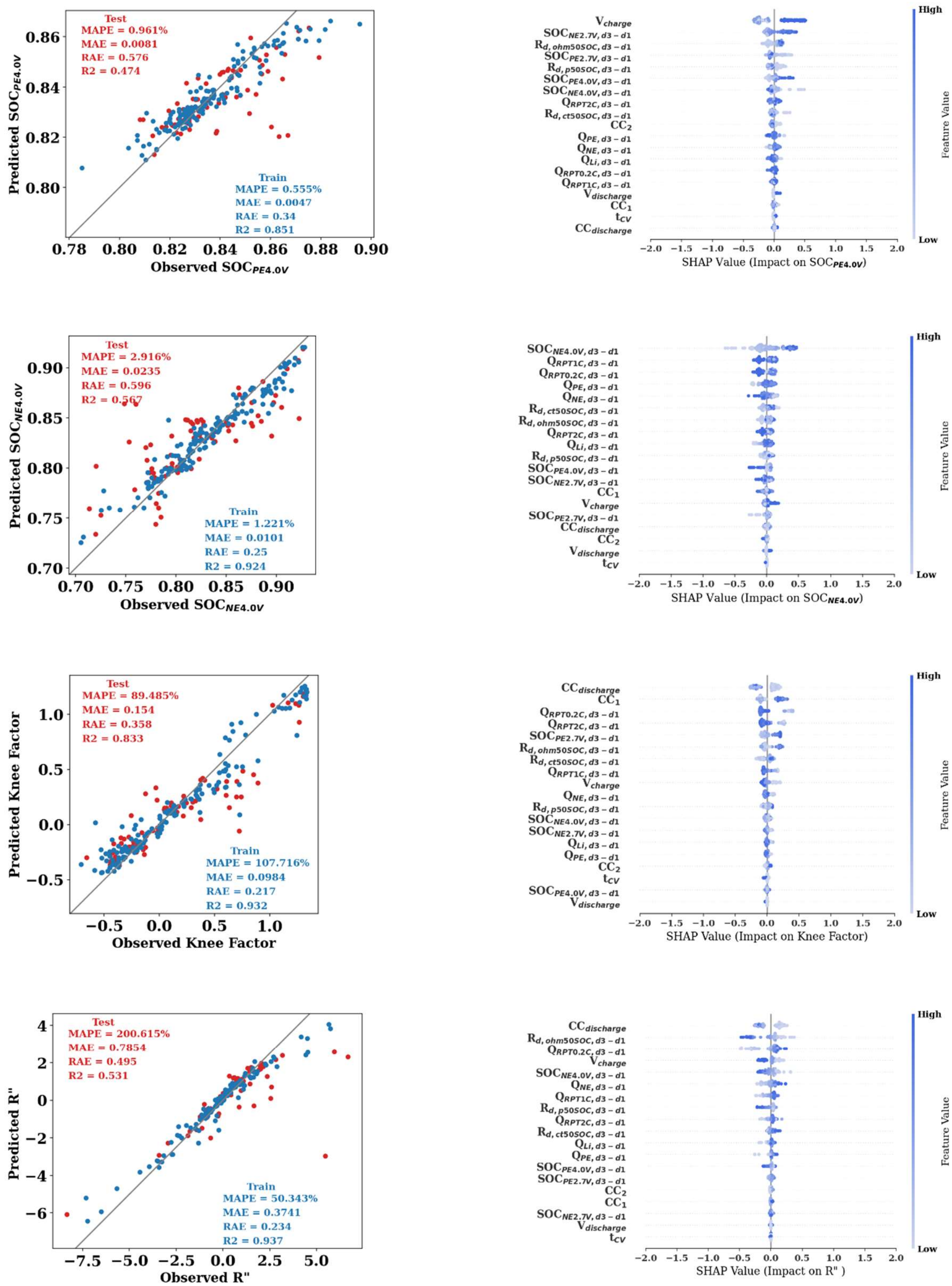
Test
MAPE = 0.961%
MAE = 0.0081
RAE = 0.576
R2 = 0.474
Train
MAPE = 0.555%
MAE = 0.0047
RAE = 0.34
R2 = 0.851
Predicted $SOC_{PE4.0V}$
Observed $SOC_{PE4.0V}$
SHAP Value (Impact on $SOC_{PE4.0V}$)
Feature Value
High
Low
Test
MAPE = 2.916%
MAE = 0.0235
RAE = 0.596
R2 = 0.567
Train
MAPE = 1.221%
MAE = 0.0101
RAE = 0.25
R2 = 0.924
Predicted $SOC_{NE4.0V}$
Observed $SOC_{NE4.0V}$
SHAP Value (Impact on $SOC_{NE4.0V}$)
Test
MAPE = 89.485%
MAE = 0.154
RAE = 0.358
R2 = 0.833
Train
MAPE = 107.716%
MAE = 0.0984
RAE = 0.217
R2 = 0.932
Predicted Knee Factor
Observed Knee Factor
SHAP Value (Impact on Knee Factor)
Test
MAPE = 200.615%
MAE = 0.7854
RAE = 0.495
R2 = 0.531
Train
MAPE = 50.343%
MAE = 0.3741
RAE = 0.234
R2 = 0.937
Predicted R"
Observed R"
SHAP Value (Impact on R")

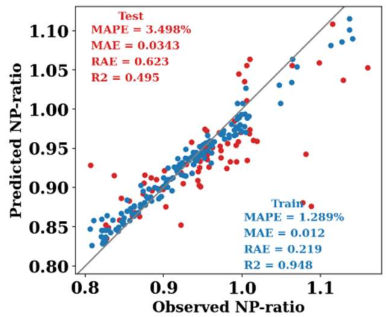
Test
MAPE = 3.498%
MAE = 0.0343
RAE = 0.623
R2 = 0.495
Train
MAPE = 1.289%
MAE = 0.012
RAE = 0.219
R2 = 0.948
Predicted NP-ratio
Observed NP-ratio
0.80
0.85
0.90
0.95
1.00
1.05
1.10
0.8
0.9
1.0
1.1

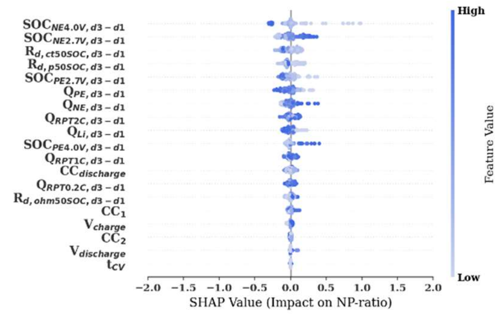
$SOC_{NE4.0V,d3-d1}$
$SOC_{NE2.7V,d3-d1}$
$R_{d,ct50SOC,d3-d1}$
$R_{d,p50SOC,d3-d1}$
$SOC_{PE2.7V,d3-d1}$
$Q_{PE,d3-d1}$
$Q_{NE,d3-d1}$
$Q_{RPT2C,d3-d1}$
$Q_{Li,d3-d1}$
$SOC_{PE4.0V,d3-d1}$
$Q_{RPT1C,d3-d1}$
$CC_{discharge}$
$Q_{RPT0.2C,d3-d1}$
$R_{d,ohm50SOC,d3-d1}$
CC_1
V_{charge}
CC_2
$V_{discharge}$
t_{CV}
−2.0 −1.5 −1.0 −0.5 0.0 0.5 1.0 1.5 2.0
SHAP Value (Impact on NP-ratio)
High
Feature Value
Low

References

[1] Jon P. Christopherson. Battery test manual for electric vehicles. Technical report, Idaho National Laboratory, U.S. Department of Energy, June 2015.

[2] Patrick Herring, Chirranjeevi Balaji Gopal, Muratahan Aykol, Joseph H. Montoya, Abraham Anapolsky, Peter M. Attia, William Gent, Jens S. Hummelshøj, Linda Hung, Ha-Kyung Kwon, Patrick Moore, Daniel Schweigert, Kristen A. Severson, Santosh Suram, Zi Yang, Richard D. Braatz, and Brian D. Storey. BEEP: A python library for battery evaluation and early prediction. *SoftwareX*, 11:100506, January 2020.

[3] Tingkai Li, Zihao Zhou, Adam Thelen, David A. Howey, and Chao Hu. Predicting battery lifetime under varying usage conditions from early aging data. *Cell Reports Physical Science*, 5(4):101891, 2024.

[4] Weiping Diao, Saurabh Saxena, and Michael Pecht. Accelerated cycle life testing and capacity degradation modeling of $LiCoO_2$-graphite cells. *Journal of Power Sources*, 435:226830, September 2019.

[5] Matthias Luh and Thomas Blank. Comprehensive battery aging dataset: capacity and impedance fade measurements of a lithium-ion NMC/C-SiO cell. *Sci. Data*, 11(1):1004, September 2024.

[6] Kristen A. Severson, Peter M. Attia, Norman Jin, Nicholas Perkins, Benben Jiang, Zi Yang, Michael H. Chen, Muratahan Aykol, Patrick K. Herring, Dimitrios Fraggedakis, Martin Z. Bazant, Stephen J. Harris, William C. Chueh, and Richard D. Braatz. Data-driven prediction of battery cycle life before capacity degradation. *Nature Energy*, 4(5):383–391, March 2019.

[7] Peter M. Attia, Aditya Grover, Norman Jin, Kristen A. Severson, Todor M. Markov, Yang-Hung Liao, Michael H. Chen, Bryan Cheong, Nicholas Perkins, Zi Yang, Patrick K. Herring, Muratahan Aykol, Stephen J. Harris, Richard D. Braatz, Stefano Ermon, and William C. Chueh. Closed-loop optimization of fast-charging protocols for batteries with machine learning. *Nature*, 578(7795):397–402, February 2020.

[8] Florian Stroebl, Ronny Petersohn, Barbara Schricker, Florian Schaeufl, Oliver Bohlen, and Herbert Palm. A multi-stage lithium-ion battery aging dataset using various experimental design methodologies. *Scientific Data*, 11(1):1020, September 2024.

[9] Jiangong Zhu, Yixiu Wang, Yuan Huang, R. Bhushan Gopaluni, Yankai Cao, Michael Heere, Martin J. Mühlbauer, Liuda Mereacre, Haifeng Dai, Xinhua Liu, Anatoliy Senyshyn, Xuezhe Wei, Michael Knapp, and Helmut Ehrenberg. Data-driven capacity estimation of commercial lithium-ion batteries from voltage relaxation. *Nature Communications*, 13(1), April 2022.

[10] Leo Wildfeuer, Alexander Karger, Deniz Aygül, Nikolaos Wassiliadis, Andreas Jossen, and Markus Lienkamp. Experimental degradation study of a commercial lithium-ion battery. *Journal of Power Sources*, 560:232498, March 2023.

[11] Joris de Hoog, Jean-Marc Timmermans, Daniel Ioan-Stroe, Maciej Swierczynski, Joris Jaguemont, Shovon Goutam, Noshin Omar, Joeri Van Mierlo, and Peter Van Den Bossche. Combined cycling and calendar capacity fade modeling of a Nickel-Manganese-Cobalt oxide cell with real-life profile validation. *Appl. Energy*, 200:47–61, August 2017.

[12] Alexis Geslin, Le Xu, Devi Ganapathi, Kevin Moy, William C Chueh, and Simona Onori. Dynamic cycling enhances battery lifetime. *Nat. Energy*, December 2024.

[13] Yuliya Preger, Heather M. Barkholtz, Armando Fresquez, Daniel L. Campbell, Benjamin W. Juba, Jessica Romàn-Kustas, Summer R. Ferreira, and Babu Chalamala. Degradation of commercial lithium-ion cells as a function of chemistry and cycling conditions. *Journal of The Electrochemical Society*, 167(12):120532, January 2020.

[14] Peter Keil and Andreas Jossen. Impact of dynamic driving loads and regenerative braking on the aging of lithium-ion batteries in electric vehicles. *J. Electrochem. Soc.*, 164(13):A3081–A3092, 2017.

[15] Yitia Chen Chen. NASA lithium ion battery dataset, 2024.

[16] Saurabh Saxena, Christopher Hendricks, and Michael Pecht. Cycle life testing and modeling of graphite/LiCoO2 cells under different state of charge ranges. *J. Power Sources*, 327:394–400, September 2016.

[17] Anup Barai, Kotub Uddin, W. D. Widanage, Andrew McGordon, and Paul Jennings. A study of the influence of measurement timescale on internal resistance characterisation methodologies for lithium-ion cells. *Scientific Reports*, 8(1), January 2018.

[18] Christoph R. Birkl, Matthew R. Roberts, Euan McTurk, Peter G. Bruce, and David A. Howey. Degradation diagnostics for lithium ion cells. *Journal of Power Sources*, 341:373–386, February 2017.

[19] Stefan Schindler and Michael A. Danzer. A novel mechanistic modeling framework for analysis of electrode balancing and degradation modes in commercial lithium-ion cells. *Journal of Power Sources*, 343:226–236, 3 2017.

[20] Matthieu Dubarry, Cyril Truchot, and Bor Yann Liaw. Synthesize battery degradation modes via a diagnostic and prognostic model. *Journal of Power Sources*, 219:204–216, December 2012.

[21] Suhak Lee, Jason B. Siegel, Anna G. Stefanopoulou, Jang-Woo Lee, and Tae-Kyung Lee. Electrode state of health estimation for lithium ion batteries considering half-cell potential change due to aging. *Journal of The Electrochemical Society*, 167:090531, 5 2020.

[22] Andrew Weng, Jason B. Siegel, and Anna Stefanopoulou. Differential voltage analysis for battery manufacturing process control. *Frontiers in Energy Research*, 11, 2023.

[23] Thomas Waldmann, Amaia Iturrondobeitia, Michael Kasper, Niloofar Ghanbari, Frédéric Aguesse, Emilie Bekaert, Lise Daniel, Sylvie Genies, Isabel Jiménez Gordon, Matthias W. Löble, Eric De Vito, and Margret Wohlfahrt-Mehrens. Review—post-mortem analysis of aged lithium-ion batteries: Disassembly methodology and physico-chemical analysis techniques. *Journal of The Electrochemical Society*, 163(10):A2149–A2164, 2016.

[24] Leo Wildfeuer, Nikolaos Wassiliadis, Alexander Karger, Fabian Bauer, and Markus Lienkamp. Teardown analysis and characterization of a commercial lithium-ion battery for advanced algorithms in battery electric vehicles. *Journal of Energy Storage*, 48:103909, April 2022.

[25] Li Yang, Boris Ravdel, and Brett L. Lucht. Electrolyte reactions with the surface of high voltage LiNi[sub 0.5]mn[sub 1.5]o[sub 4] cathodes for lithium-ion batteries. *Electrochemical and Solid-State Letters*, 13(8):A95, 2010.

[26] L. Somerville, J. Bareño, P. Jennings, A. McGordon, C. Lyness, and I. Bloom. The effect of pre-analysis washing on the surface film of graphite electrodes. *Electrochimica Acta*, 206:70–76, July 2016.

[27] Matthieu Dubarry, Cyril Truchot, and Bor Yann Liaw. Cell degradation in commercial $LiFePO_4$ cells with high-power and high-energy designs. *Journal of Power Sources*, 258:408–419, July 2014.

[28] Johannes Philipp Fath, Daniel Dragicevic, Laura Bittel, Adnan Nuhic, Johannes Sieg, Severin Hahn, Lennart Alsheimer, Bernd Spier, and Thomas Wetzel. Quantification of aging mechanisms

and inhomogeneity in cycled lithium-ion cells by differential voltage analysis. *J. Energy Storage*, 25(100813):100813, October 2019.

[29] Julius Schmitt, Markus Schindler, Andreas Oberbauer, and Andreas Jossen. Determination of degradation modes of lithium-ion batteries considering aging-induced changes in the half-cell open-circuit potential curve of silicon–graphite. *Journal of Power Sources*, 532:231296, 2022.

[30] Johannes Sieg, Mathias Storch, Johannes Fath, Adnan Nuhic, Jochen Bandlow, Bernd Spier, and Dirk Uwe Sauer. Local degradation and differential voltage analysis of aged lithium-ion pouch cells. *J. Energy Storage*, 30(101582):101582, August 2020.

[31] Matthieu Dubarry and David Beck. Perspective on mechanistic modeling of Li-ion batteries. *Accounts of Materials Research*, 3(8):843–853, June 2022.

[32] Matthieu Dubarry and George Baure. Perspective on commercial Li-ion battery testing, best practices for simple and effective protocols. *Electronics*, 9(1):152, January 2020.

[33] Peter M. Attia, Alexander Bills, Ferran Brosa Planella, Philipp Dechent, Gonçalo dos Reis, Matthieu Dubarry, Paul Gasper, Richard Gilchrist, Samuel Greenbank, David Howey, Ouyang Liu, Edwin Khoo, Yuliya Preger, Abhishek Soni, Shashank Sripad, Anna G. Stefanopoulou, and Valentin Sulzer. Review—"Knees" in lithium-ion battery aging trajectories. *Journal of The Electrochemical Society*, 169(6):060517, June 2022.

[34] Paula Fermín-Cueto, Euan McTurk, Michael Allerhand, Encarni Medina-Lopez, Miguel F. Anjos, Joel Sylvester, and Gonçalo dos Reis. Identification and machine learning prediction of knee-point and knee-onset in capacity degradation curves of lithium-ion cells. *Energy and AI*, 1:100006, August 2020.

[35] Roland Jung, Michael Metzger, Filippo Maglia, Christoph Stinner, and Hubert A. Gasteiger. Oxygen release and its effect on the cycling stability of $LiNi_xMn_yCo_zO_2$ (NMC) cathode materials for Li-ion batteries. *Journal of The Electrochemical Society*, 164(7):A1361–A1377, 2017.

[36] Alexis Geslin, Bruis van Vlijmen, Xiao Cui, Arjun Bhargava, Patrick A. Asinger, Richard D. Braatz, and William C. Chueh. Selecting the appropriate features in battery lifetime predictions. *Joule*, 7(9):1956–1965, 2023.